CODEN:LUTEDX/(TEIE-5504)/1-64/(2023)

Industrial Electrical Engineering and Automation

# Sensorless Field-Oriented Control and Position Estimation

## A thesis presented for the degree of Master of Science in Electrical Engineering

**Roberts Bitenieks, Lars Brander**

Division of Industrial Electrical Engineering and Automation
Faculty of Engineering, Lund University

# Sensorless Field-Oriented Control and Position Estimation

A thesis presented for the degree of
Master of Science in Electrical Engineering


LUNDS UNIVERSITET

Roberts Bitenieks, bi3450ro-s@student.lu.se
Lars Brander, la7853br-s@student.lu.se

Supervisor: Mats Alaküla, mats.alakula@iea.lth.se
Examiner: Francisco J. Marquez-Fernández, fran.marquez@iea.lth.se

Industrial Electrical Engineering and Automation
Lund University
Sweden

June 2023

# Abstract

This master's thesis investigates the feasibility of implementing field-oriented control for a *BLDC* motor without relying on a position sensor from a standstill up to 400 rad/s. To achieve this objective, various approaches were used at standstill and high speeds. The high-frequency injection method was used at standstill and lower speeds, while a method based on estimated magnetic flux was utilized at higher speeds to estimate the position of the rotor. To evaluate these methods, model-based programming in *Matlab* and *Simulink* was done. The crucial aspects of these methods are elaborated in detail in this thesis work. For real-time execution, the implementation was converted into C code using *TargetLink* and subsequently flashed onto the *ECU*. This master's thesis was performed in collaboration with *BorgWarner Sweden AB* in Landskrona, Sweden.

# Acknowledgements

Firstly, we would like to express our great gratitude to our supervisor, Prof. Mats Alaküla, from the Department of Industrial Electrical Engineering and Automation at the Faculty of Engineering at Lund University. His guidance, support and expertise throughout the entire master thesis was very valuable and greatly appreciated. Without his insightful suggestions and constructive feedback, this thesis would not have been possible. Secondly, we would like to thank BorgWarner Sweden AB for the great opportunity to conduct our master thesis with them. A special thanks to our supervisors Meike Rönn and Arne Hörberg for providing valuable suggestions, ideas and equipment.

# Contents


**1 Introduction** **1**
- 1.1 Background . . . 1
- 1.2 Literature review . . . 2
- 1.3 Master thesis goals . . . 2
  - 1.3.1 Rationale for topic selection . . . 2
  - 1.3.2 Limitations . . . 2

**2 Theory** **3**
- 2.1 Field oriented control - FOC . . . 3
  - 2.1.1 The Clarke transform . . . 3
  - 2.1.2 The Park transform . . . 4
- 2.2 BLDC motor . . . 4
- 2.3 BEMF based methods . . . 5
  - 2.3.1 Magnetic flux based rotor position estimation . . . 6
- 2.4 High-frequency injection method . . . 7
- 2.5 Single phase-locked loop . . . 10
- 2.6 Polar to Cartesian coordinate conversion . . . 12
- 2.7 Discrete filters . . . 12
  - 2.7.1 Low-pass filter . . . 12
  - 2.7.2 Bandpass filter . . . 13

**3 Experimental equipment** **16**
- 3.1 Hardware . . . 16
  - 3.1.1 Rig . . . 16
  - 3.1.2 BLDC motor . . . 17
  - 3.1.3 ECU . . . 19
- 3.2 Software . . . 19
  - 3.2.1 CANalyzer . . . 20

**4 Method** **21**
- 4.1 Implemented software . . . 21
- 4.2 Implementation of the magnetic flux based method . . . 22
  - 4.2.1 Phase voltage estimation . . . 22
  - 4.2.2 The Clarke transform . . . 22
  - 4.2.3 BEMF estimation . . . 23
  - 4.2.4 Magnetic flux calculation . . . 24
  - 4.2.5 Angle estimation with PLL . . . 25
- 4.3 Implementation of high-frequency based rotor position estimation 29

**5 Results** **37**
- 5.1 Rotor angle estimation using the high-frequency injection method 37
- 5.2 Rotor angle estimation using the magnetic flux method . . . 38
- 5.3 Transition between the two estimation methods . . . 39
- 5.4 Torque and speed performance . . . 39

5.5 Direct and quadrature currents . . . . . 40
5.5.1 Plots of the direct and quadrature currents . . . . . 40
5.5.2 Estimated angle based on d-q plots . . . . . 44
5.6 High-frequency current response . . . . . 45

**6 Discussion** **46**
6.1 BEMF-based methods . . . . . 46
6.1.1 The two-argument arctangent method . . . . . 46
6.1.2 QPLL method . . . . . 46
6.1.3 PLL method . . . . . 47
6.2 High-frequency method . . . . . 48
6.3 Hardware and previously implemented software . . . . . 49

**7 Conclusion and future work** **50**
7.1 Conclusion . . . . . 50
7.2 Future work . . . . . 50

**8 References** **51**

**9 Appendix** **53**
9.1 Appendix A - Simulink implementation . . . . . 53

# Acronyms

**BEMF** Back Electro-Motive Force
**BLDC** Brushless Direct Current
**BPF** Bandpass filter
**ECU** Electronic control unit
**FOC** Field-oriented control
**HF** High-frequency
**LPF** Low-pass filter
**PLL** Phase locked loop
**PFD** Phase frequency detector
**RPM** Revolutions per minute

# 1 Introduction

This thesis aims to investigate the possibility to estimate the rotor position of a brushless direct current (BLDC) motor at standstill and higher speeds. Subsequently, the identified methods will be implemented in a field-oriented control model provided by BorgWarner Sweden AB. The performance of the sensorless methods will be compared to a sensored implementation based on measured torque.

## 1.1 Background

BorgWarner is an automotive supplier that specializes in developing various technology solutions for combustion, hybrid, and electric vehicles. Several of these solutions use actuators with BLDC motors for applications such as mechanical actuation, namely, moving a shaft to a certain position or a hydraulic application where a BLDC motor actuates an oil pump.

The hydraulic application is currently implemented using block commutation control strategy which does not require knowledge of the rotor position. However, in a new implementation, BorgWarner intends to transition to a field oriented control (FOC) strategy, even for hydraulic applications, where a position sensor is not present. The transition is motivated by the need to reduce the reliance on rare earth metals used in the angle sensor setup. Additionally, the sensor elimination will save space in hardware and reduce costs.

Figure 1: A hydraulic application where a BLDC motor actuates an oil pump. Picture from BorgWarner Sweden AB.

## 1.2 Literature review

In order to estimate the rotor position, various methods are utilized. However, as evidenced by the studied papers, two main methods are primarily employed (Wenjun, Shaocheng, Jinghong, Hongrui, and Xiaona 2021), (Xiaocheng, Liang, Zijian, Yuchen, and Pengjie 2022) and (Song, Han, Zheng and Chen, 2018). At medium and high speeds, the back electromotive force (BEMF) is utilized (Abo-Khalil 2020) and (Gieras, Wang and Kamper 2008). However, at standstill and lower speeds, where the electromotive force is negligible or absent, the saliency characteristics of the motor along with high-frequency induced voltage signals are used to determine the rotor position (Surroop, Combes, Martin and Rouchon 2020), (Shujin, Baozhu, Zhengyun, Fei, and Huade 2006). Therefore, this thesis aims to investigate the feasibility of implementing the two methods for rotor position estimation: the high-frequency induced voltage signals method and the BEMF-based method.

## 1.3 Master thesis goals

The primary objective of this master's thesis is to explore the possibilities of estimating the rotor position of the BLDC motor at standstill and speeds up to 400 rad/s. Subsequently, the current model will be updated with the newly developed position estimation methods. The performance of these methods in terms of torque output will be compared to the existing FOC implementation with a position sensor.

### 1.3.1 Rationale for topic selection

The selection of this thesis subject is driven by a keen interest in electric motors and their control, as well as the desire to expand knowledge in this area. Conducting the thesis at BorgWarner Sweden AB is a valuable opportunity to deepen understanding in the electric motor control and apply previously acquired knowledge from power electronics, control engineering and digital signal processing.

### 1.3.2 Limitations

This thesis mainly focuses on implementing sensorless angle estimation methods within the field-oriented control for rotor positions ranging from standstill up to 400 rad/s. The scope of this work does not include the optimization of the provided FOC model, nor does it involve any modifications to the hardware of the BLDC motor.

# 2 Theory

This section provides an overview of the theory used to develop the magnetic flux based method and the high-frequency injection method for obtaining the rotor position without a position sensor.

## 2.1 Field oriented control - FOC

Field-oriented control, also known as vector control, is a technique used in AC and BLDC motor control. FOC enables precise control of the motor's torque and speed by dividing the stator current $i_s$ into two components: the direct current $i_d$ and the quadrature current $i_q$. Figure 2 illustrates the direct torque control of the BLDC motor.

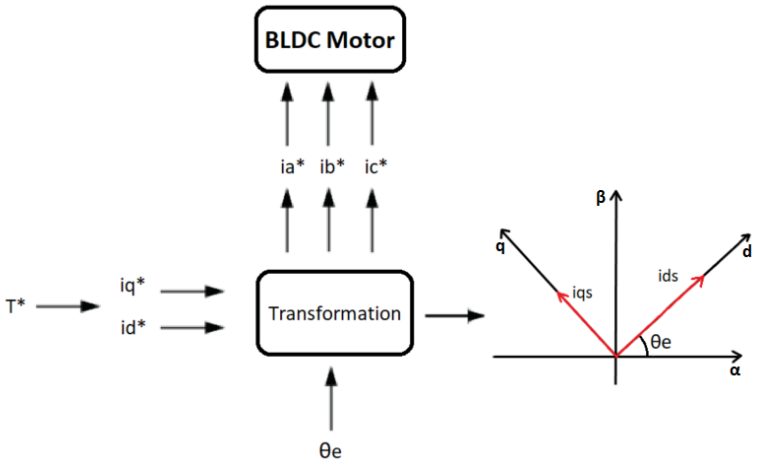


Figure 2: Direct torque control with FOC.

To utilize the FOC control technique, a rotating reference frame is required. In power electronics, this reference frame is called Park transform. It introduces a dq-plane, where the d-axis aligns with the rotor's flux vector, and the q-axis is perpendicular to the rotor flux. The rotor angle position ($\theta$) is required for operating within this system.

### 2.1.1 The Clarke transform

The Clarke transform, also known as the $ABC$ to $\alpha\beta$-transform, is used to simplify the calculation of the three-phase system. The Clarke transform is also necessary for calculating the Park transform. In this work, the amplitude-invariant Clarke transformation is utilized (Alaküla, Bängtsson and Karlsson

2019). Equation 1 describes the general amplitude-invariant Clarke transformation (O'Rourke, Qasim, Overlin, Hongrui, and Kirtley 2019).

$$\begin{bmatrix} s_\alpha \\ s_\beta \\ s_0 \end{bmatrix} = \frac{2}{3} \begin{bmatrix} 1 & -\frac{1}{2} & -\frac{1}{2} \\ 0 & \frac{\sqrt{3}}{2} & -\frac{\sqrt{3}}{2} \\ \frac{1}{2} & \frac{1}{2} & \frac{1}{2} \end{bmatrix} \begin{bmatrix} s_a \\ s_b \\ s_c \end{bmatrix} \tag{1}$$

### 2.1.2 The Park transform

From the $\alpha\beta$-plane, the rotating dq-reference plane can be defined by assuming that the rotor angle $\theta$ is known (Alaküla, Bängtsson and Karlsson 2019). Equation 2 describes the relationship between $\alpha\beta$- and dq-plane.

$$\begin{cases} s_d = s_\alpha \cdot cos(\theta) + s_\beta \cdot sin(\theta) \\ s_q = s_\beta \cdot cos(\theta) - s_\alpha \cdot sin(\theta) \end{cases} \tag{2}$$

## 2.2 BLDC motor

A brushless DC-motor (BLDC) can be modelled using three single-phase load models, where each phase consists of a resistance, an inductance and an induced electromotive force connected in series, as shown in figure 3:

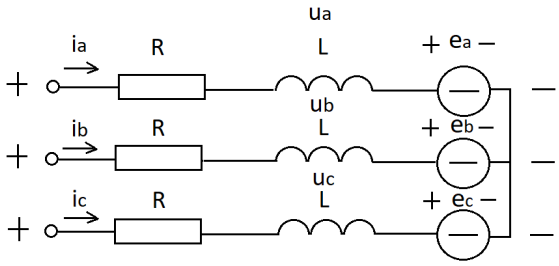


Figure 3: Three-phase load model.

Mathematically, each single phase can be represented as:

$$u = R \cdot i + L \cdot \frac{di}{dt} + e \tag{3}$$

where $R$ is the phase resistance, $L$ is the phase inductance, $i$ is the current, $\frac{di}{dt}$ is the rate of change of the current $i$ and $e$ is the induced voltage.

In theory, the load model of a BLDC motor should generate a sinusoidal BEMF waveform. However, BLDC motors have a trapezoidal BEMF waveform. This

characteristic is a result of the BLDC motor's design, which consists of magnets with parallel magnetization, thereby achieving a constant amplitude of the magnetic flux density along the air gap. Theoretically, if the back electromotive force waveform of a BLDC motor is a perfect trapezoid, it would result in a 15% higher power density compared to a permanent magnet synchronous motor with a sinusoidal BEMF waveform (Sang-Hoon, 2017). Figure 4 illustrates the BEMF waveform of the studied BLDC motor at 500 rpm under no-load conditions.

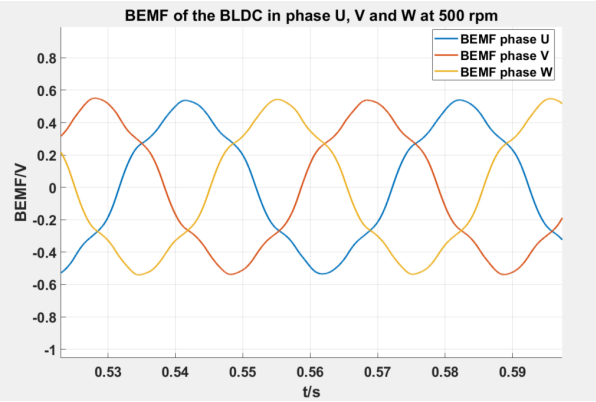


Figure 4: BEMF waveform of the studied BLDC motor at 500 rpm and no-load conditions.

## 2.3 BEMF based methods

The back electromotive force can be used to obtain the rotor position at medium and high speeds (Gieras, Wang and Kamper 2008). The theory behind this method is explained by expressing the single-phase load equation 3 in $\alpha\beta$-plane:

$$\overrightarrow{v}_{\alpha\beta} = L \cdot \frac{d\overrightarrow{i_{\alpha\beta}}}{dt} + R \cdot \overrightarrow{i_{\alpha\beta}} + \overrightarrow{e}_{\alpha\beta} \tag{4}$$

where $\overrightarrow{e}$ is expressed as:

$$\overrightarrow{e} = j \cdot \omega_r \cdot \overrightarrow{\Psi}_m \tag{5}$$

The quantities such as the inductance L, the resistance R and the magnetic flux from the permanent magnet $\Psi_m$ are known, and the current $i_{\alpha\beta}$ and voltage $v_{\alpha\beta}$ can be measured or estimated. Therefore, by solving equation 4 for the BEMF, which also holds the information about the angular electrical rotor speed $\omega_r$, the rotor position can be determined. Equation 6 represents the calculation of the BEMF based on the single-phase load model.

$$\overrightarrow{e} = \overrightarrow{v_{\alpha\beta}} - L \cdot \frac{d\overrightarrow{i_{\alpha\beta}}}{dt} - R \cdot \overrightarrow{i_{\alpha\beta}} \tag{6}$$

### 2.3.1 Magnetic flux based rotor position estimation

An alternative approach to estimating the rotor position is by utilizing the magnetic flux instead of BEMF. Figure 5 illustrates the relationship between the magnetic flux vector and the rotor position:

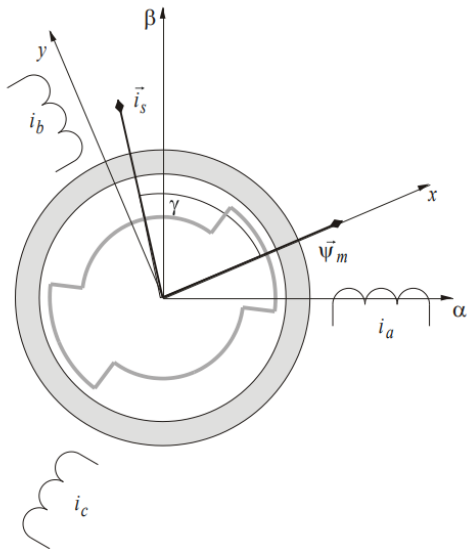


Figure 5: Three phase armature winding (Alaküla, Bängtsson and Karlsson 2019).

Mathematically, the relationship between the BEMF and the magnetic flux can be described as:

$$\begin{cases} \Psi_{s\alpha} = \int e_\alpha \cdot dt = \int (v_\alpha - R \cdot i_\alpha) \cdot dt \\ \Psi_{s\beta} = \int e_\beta \cdot dt = \int (v_\beta - R \cdot i_\beta) \cdot dt \end{cases} \tag{7}$$

where $\Psi_{s\alpha}$ and $\Psi_{s\beta}$ represent the stator flux-linkages in $\alpha\beta$-plane, $v_\alpha$, $v_\beta$, $i_\alpha$ and $i_\beta$ denote voltages and currents in $\alpha\beta$-plane (Peilin Xu 2017).

Since the control system provided by BorgWarner sets the direct armature current to zero and only uses the quadrature current:

$$\begin{cases} i_d^* = 0 \\ i_q* = \frac{T^*}{\Psi_m} \end{cases} \tag{8}$$

the power factor between the BEMF and stator current becomes free variables, potentially resulting in a large angle $\varphi$. This is undesirable, as the power factor

should ideally be as close to 1 as possible (Alaküla, Bängtsson and Karlsson 2019). The behaviour described can be observed in figure 6.

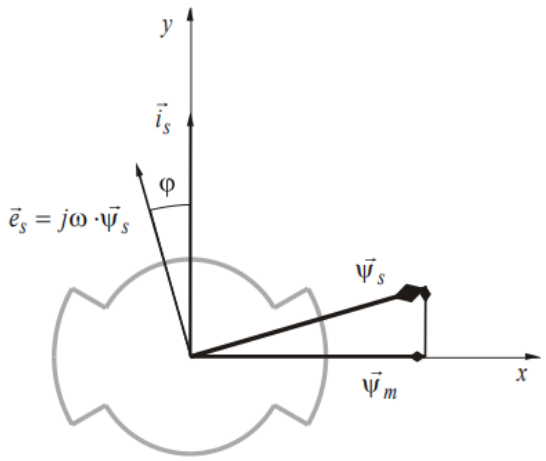


Figure 6: The power factor $cos(\varphi)$ can be obtained from the angle $\varphi$ between the stator current $\overrightarrow{i_s}$ and the BEMF $\overrightarrow{e_s}$ (Alaküla, Bängtsson and Karlsson 2019).

It is worth noting that the stator flux vector $\overrightarrow{\Psi}_s$ is not ideally aligned to d-axis. To compensate for this, the following equation is used 9:

$$\overrightarrow{\Psi}_m = \overrightarrow{\Psi}_s - \overrightarrow{i}_s \cdot L \tag{9}$$

Hence, the rotor position can now directly be extracted from the magnetic flux $\overrightarrow{\Psi}_m$.

## 2.4 High-frequency injection method

The high-frequency signal injection method is applied to estimate the rotor position at standstill and low speeds (Surroop, Combes, Martin, & Rouchon, 2020). This is possible due to the physical phenomenon of the BLDC motor, namely, that the reluctance along the d-axis is usually greater than the reluctance along the q-axis. The d-axis is aligned with the magnetic poles of the rotor while the q-axis is perpendicular to the d-axis. Since the magnetic flux in the BLDC motor is generated by the permanent magnets, the reluctance will be bigger once the stator windings align with the magnets, creating a stronger magnetic linkage in the d-axis than in the q-axis (Sang-Hoon 2017). Figure 7 illustrates the variation in inductance depending on the rotor position during one electrical period.

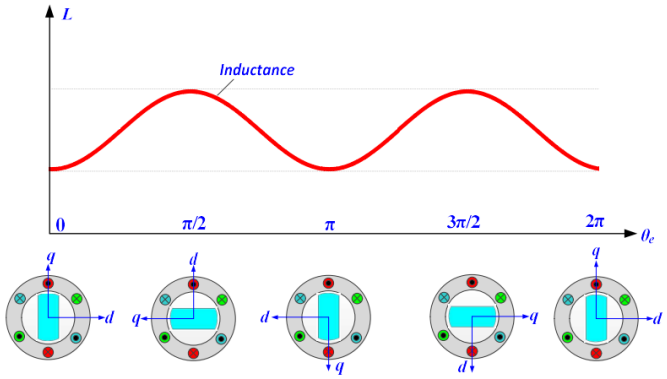


Figure 7: Inductance variation with rotor position (Peilin Xu 2017).

To benefit from the differences in $L_d$ and $L_q$, high-frequency voltage signals are injected into the $\alpha\beta$-plane and can be described as:

$$\begin{cases} u_\alpha = u_{hf} \cdot cos(\omega_{hf} \cdot t) \\ u_\beta = u_{hf} \cdot sin(\omega_{hf} \cdot t) \end{cases} \tag{10}$$

where $u_{hf}$ is the amplitude of the injected voltage signal and $\omega_{hf}$ is the angular frequency of the injected signal.

The HF-injected voltage signals result in the following current response in the $\alpha$ and $\beta$ components:

$$i_\alpha + j i_\beta = \frac{u_{hf}}{2\omega_{hf} L_d L_q} \left( (L_d + L_q) e^{j(\omega_{hf} t - \frac{\pi}{2})} + (-L_d + L_q) e^{j(-\omega_{hf} t + 2 \cdot \theta_e + \frac{\pi}{2})} \right) \tag{11}$$

where $i_\alpha$ and $i_\beta$ are the current responses in $\alpha\beta$-plane, $L_d$ and $L_q$ are d and q axis inductances and $\omega_{hf}$ is the angular frequency of the injection (Peilin Xu 2017).

When combined, $u_\alpha$ and $u_\beta$ form a small circle on top of the control vector, as depicted in figure 9. These injected signals compose a rotating voltage that induces a rotating magnetic flux in the rotor, as illustrated in figure 8. Since the amplitude of the voltage is constant, the magnetic flux is constant as well. At standstill, the smaller circle is centered around the origin and gradually moves away from origin as the speed increases.

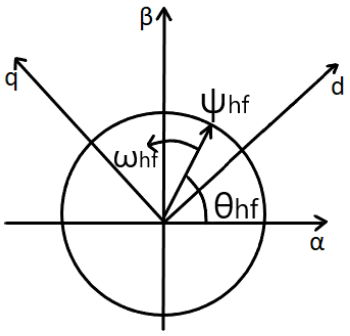


Figure 8: This figure shows the circle that is created by the HF-injected voltage signals at standstill.

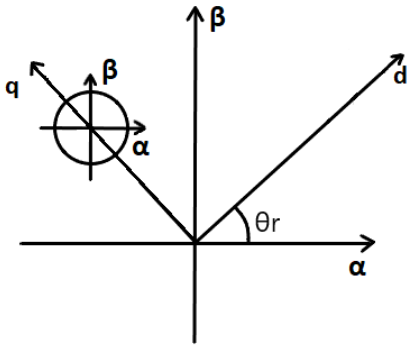


Figure 9: This figure illustrates the $\alpha\beta$-plane with HF voltage signals creating a circle on top of the voltage control vector. Here, the rotor is rotating at some speed $\omega_r$.

The characteristic shown in figure 7 results in an ellipsoidal high-frequency current response when observed in the $\alpha\beta$-plane. Assuming that the rotor is displaced at some angle $\theta_r$ during standstill, the high-frequency current response due to HF-injection is illustrated in figure 10:

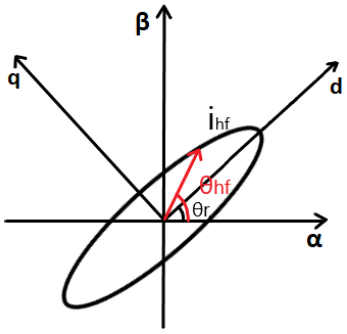


Figure 10: The current response at standstill in $\alpha\beta$-plane due to the HF voltage signal injection.

The amplitude of the high-frequency current $i_{hf}$ in figure 10 can now be utilized to determine the direction of the d-axis and, consequently, the position of the rotor. To achieve this, the angle of the high-frequency flux vector $\overrightarrow{\Psi_{hf}}$ in figure 8 is required, as the amplitude of the high-frequency current response depends on the HF flux vector. The simplest approach to determine the rotor position using this analogy is to observe the high-frequency current response $i_{hf}$ and identify the high-frequency current peaks. These peaks correspond to the points where the high-frequency current vector in figure 10 has the greatest distance from the origin. However, as shown in figure 7, this method yields two points during one HF injection period where the high-frequency current response has its highest values, namely, at +d-axis and at -d-axis (Teske 2001).

## 2.5 Single phase-locked loop

A single phase-locked loop (PLL) enables the system to approximate the phase angle of an unknown sinusoidal function. The main components of a PLL include the *Phase Frequency Detector* (PFD), controller, angle integrator and signal-to-square wave converter. Figure 11 provides an overview of the PLL.

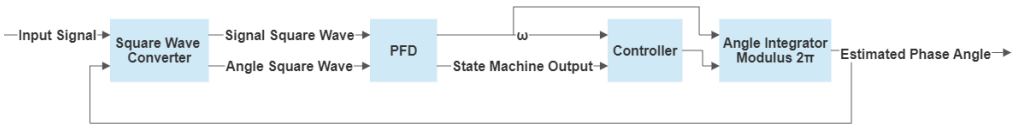


Figure 11: Overview of the PLL.

The input to the PLL is the signal, and the output is the estimated phase angle. The PLL operates in several steps. In the first step, both the signal and the angle are converted into square waves. The signal square wave is 1 when the signal is $> 0$ and the angle square wave is 1 when the angle is $> \pi$. The PLL will try to align the signal square wave perfectly with the angle square wave. To achieve this, it uses a PFD, and the state machine of this PFD is shown in figure 12. The PFD also estimates the frequency of the signal.

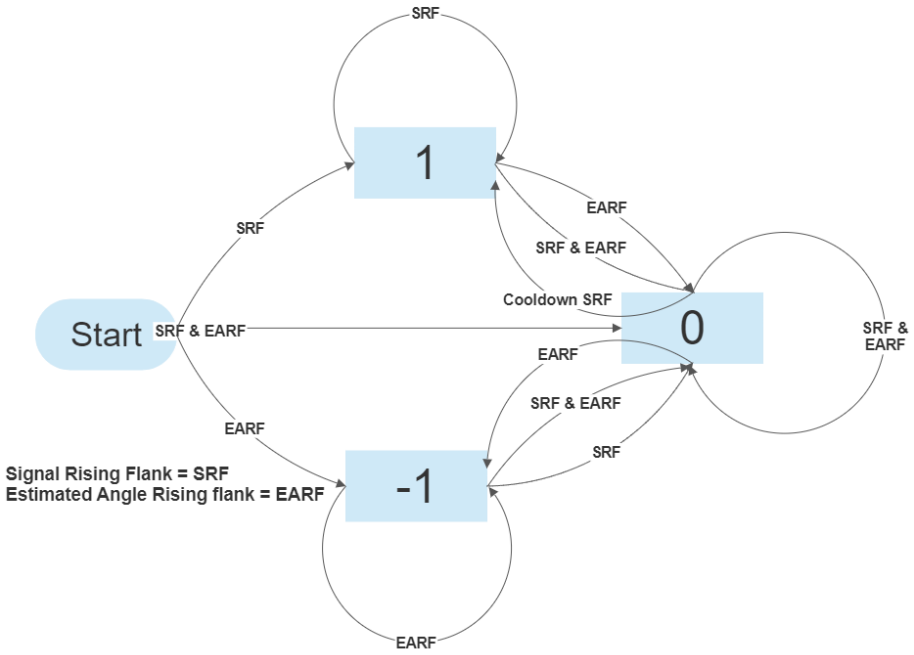


Figure 12: State machine in the PFD. The output (-1, 0 or 1) is sent to the controller. An output of -1 causes the angle estimation to slow down, allowing the signal to catch up with the estimation. An output of 0 maintains the same frequency for the angle estimation as the signal. An output of 1 causes the angle estimation to accelerate in order to catch up with the signal.

The outputs from the state machine and the estimated frequency from the PFD are sent as inputs to the controller. The output of the controller along with $\omega$ is integrated to obtain the estimated angle.

## 2.6 Polar to Cartesian coordinate conversion

To process an angle $\alpha$ in the range between 0 and $2\pi$, polar to Cartesian coordinate conversion is necessary. This conversion splits the angle into the in-phase (real) and quadrature (imaginary) components. This is shown in equation 12. The need for this conversion arises due to the discontinuity exhibited by the polar angle.

$$\begin{cases} I = \cos\alpha \\ Q = \sin\alpha \end{cases} \tag{12}$$

In Cartesian form, the angle no longer exhibits discontinuity and can be processed accurately. The conversion from Cartesian to Polar angle can be seen in equation 13.

$$\alpha^* = \arctan 2(\frac{Q}{I}) \tag{13}$$

For the Cartesian-to-polar coordinate conversion method to calculate the correct angle, it is assumed that the *arctan2* function detects the quadrant in which the angle is located (Torrence B.F and Torrence E. 1999).

## 2.7 Discrete filters

In control engineering, discrete filters are used to reduce unwanted noise from sampled signals and/or enhance or reduce a specific frequency before further processing within the control loop.

### 2.7.1 Low-pass filter

For the purpose of reducing unwanted noise from the measured phase current signals, 1st order low-pass filters are applied in this work. The discrete transfer function of a 1st order low-pass filter with zero-order hold can be described by the following equation 14:

$$H(z) = \frac{Y(z)}{X(z)} = \frac{1 - e^{-\omega_c \cdot T}}{z - e^{-\omega_c \cdot T}} \tag{14}$$

where $\omega_c$ represents the cutoff angular frequency and $T$ is the sample time (Rusek 2021). Inserting $\omega_c = 10$ [rad/s] and $T = 0.0001$ [s] into equation 14 yields the frequency response illustrated in figure 13 and the corresponding Bode plot of this filter is illustrated in figure 14.

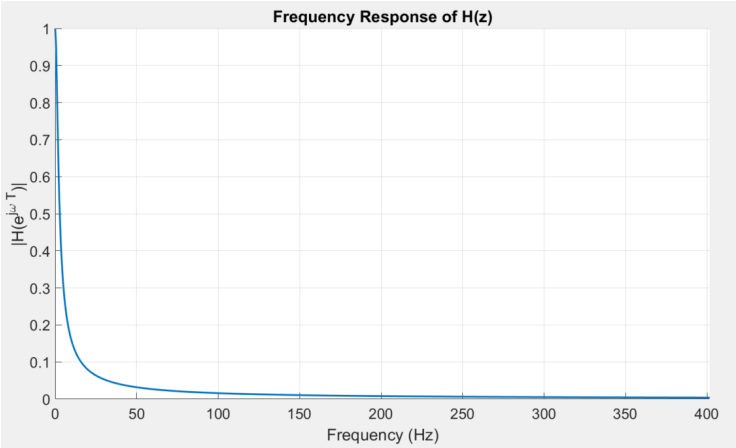


Figure 13: The frequency response of the 1st order discrete low-pass filter.

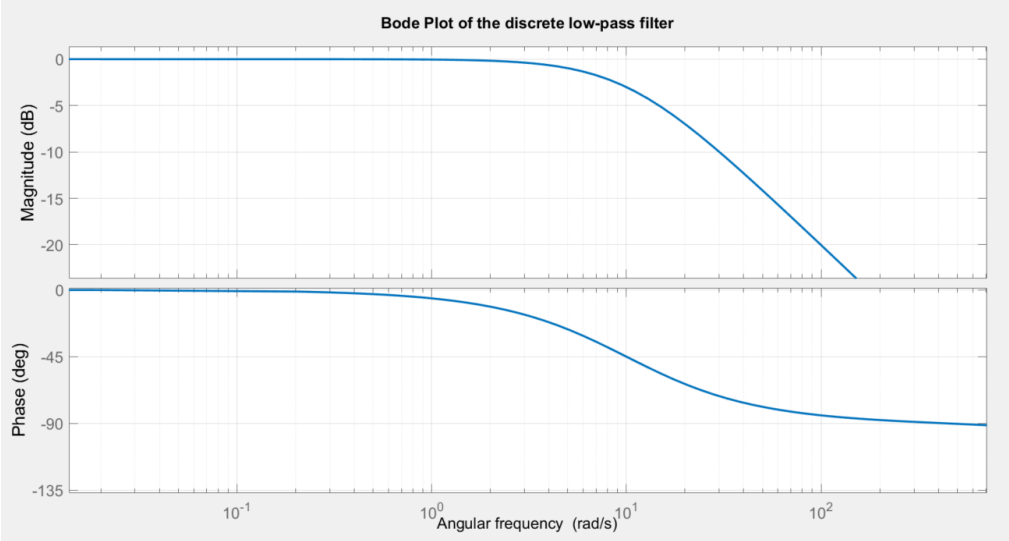


Figure 14: The bode plot of the 1st order discrete low-pass filter.

### 2.7.2 Bandpass filter

Another type of discrete filter used in the methods of this work is a bandpass filter, which allows only a specific frequency range to pass through. This filter is used in the high-frequency method to observe the phase current response at a specific frequency due to signal injection. The general z-domain discrete transfer

function for a bandpass filter is given by:

$$H(z) = \frac{b_0 + b_1 z^{-1} + ... + b_{M-1} z^{-(M-1)}}{1 + a_1 z^{-1} + ... + a_{N-1} z^{-(N-1)}}$$

where $b_0$, $b_1$, $b_{M-1}$, $a_1$ and $a_{N-1}$ are the polynomial coefficients, with $N \geq M$. The coefficients of a 2nd order bandpass filter are determined using *Iterative Filter Design*, changing the coefficients until the desired filter properties where achieved. This is resulting in the following z-domain transfer function (Rice M):

$$H_{BPF}(z) = \frac{0.015 + 0.015 z^{-2}}{1 - 1.903 z^{-1} + 0.9702 z^{-2}} \tag{15}$$

The corresponding frequency response is shown in figure 15, which demonstrates that the peak of the curve corresponds to the center frequency of 416.67 [Hz] with a gain of 1.

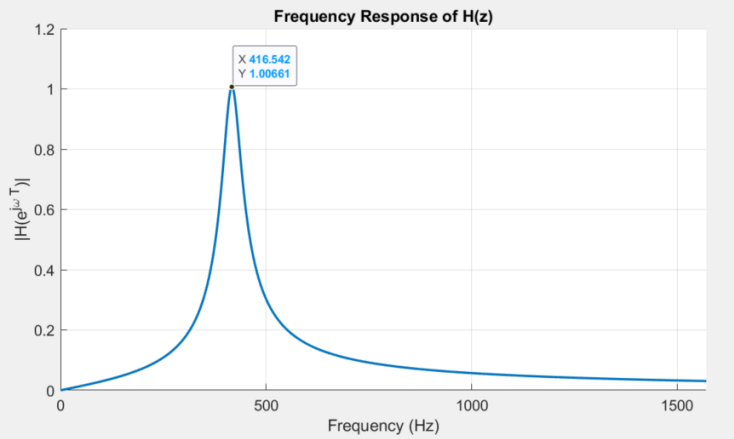


Figure 15: The frequency response of the derived discrete bandpass filter.

Additionally, the pole-zero plot of the bandpass filter derived from equation 15 is illustrated in figure 16:

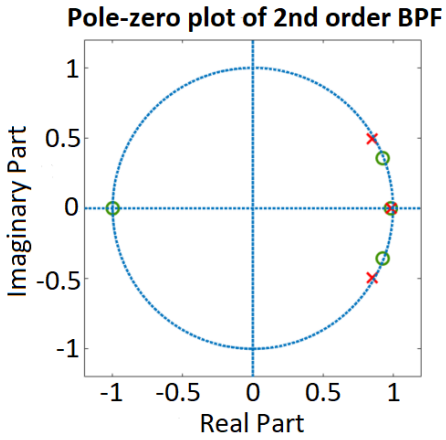


Figure 16: The pole-zero plot of the bandpass filter with the transfer function presented in equation 15.

# 3 Experimental equipment

The experimental equipment is divided into two parts, namely, the hardware part and the software part. The main parts of each are presented in this chapter.

## 3.1 Hardware

This section provides an overview of the hardware used in this thesis work.

### 3.1.1 Rig

The experimental setup includes a motor fixture, servo drive, and a measurement computer. The motor fixture and servo drive are placed on top of a cabinet, while the measurement computer is connected to the rig via USB and Ethernet. Figure 17 shows the motor fixture and servo drive setup and figure 18 shows the power supply in more detail.

Figure 17: Motor fixture and servo drive setup. The measurement computer is placed on top of the cabinet and connected to the rig via USB and Ethernet. The inside of the cabinet consists of the power supply, power electronics to drive the servo motor and fuses.


Figure 18: The power supply used to power the BLDC motor is a *Delta Elektronika SM 52-AR-60* power supply.

### 3.1.2 BLDC motor

The experimental setup includes a BLDC motor. The motor is modified with cables connected to the motor phases to measure phase currents. Figure 19 shows the modified BLDC motor, and figure 20 shows the complete fixture, including the BLDC motor, torque sensor, servo motor, and phase current sensor.

Figure 19: The modified BLDC motor with cables going to and from phases to measure phase currents.

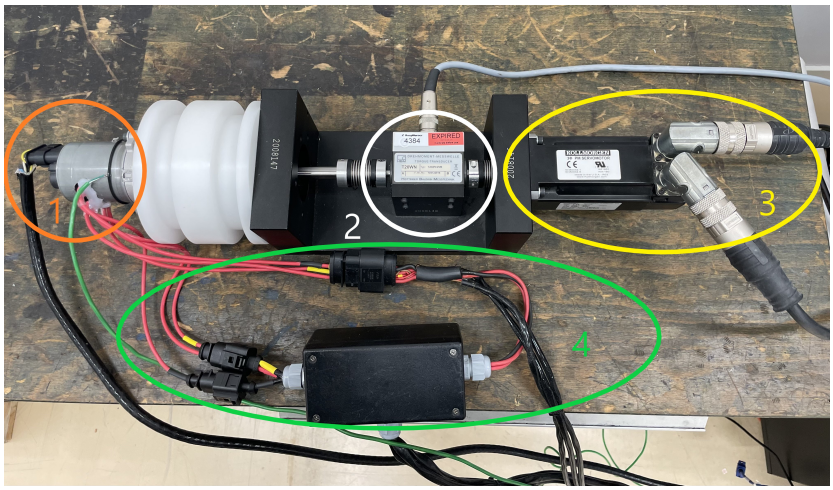


Figure 20: The complete fixture including the BLDC motor (1), the torque sensor (2), the servo motor (3) and the phase current sensor (4).

Some properties of the BLDC motor are stated below:

$$
\begin{aligned}
R_{phase} &= 0.07604\Omega \\
L_d &\approx 0.074mH \\
L_q &\approx 0.119mH \\
&3 \text{ pole pairs}
\end{aligned}
$$

A figure of the d and q inductances generated from *Ansys Motor-CAD* of this specific motor and handed over from Líder Xavier García Parrales, MSc in Electrical Engineering, can be seen in figure 21.

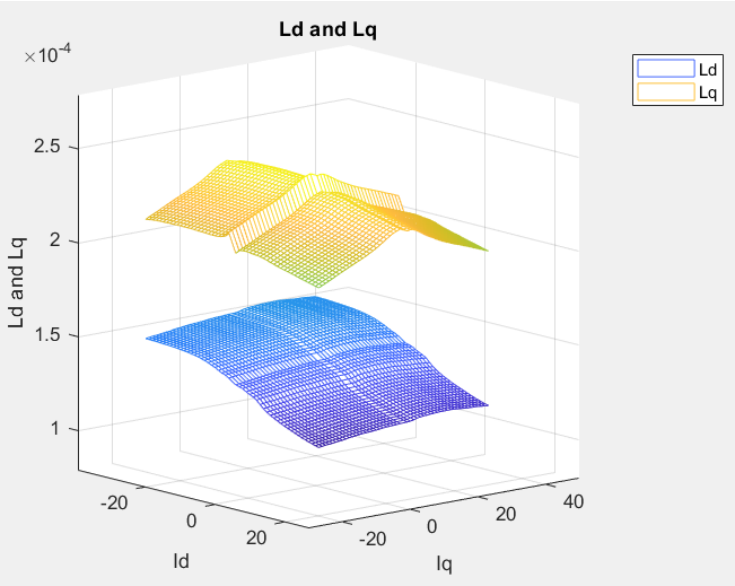


Figure 21: The relation between $L_d$ and $L_q$ in the motor can be seen as a function of $i_d$ and $i_q$ currents.

### 3.1.3 ECU

In figure 22 the ECU is shown when disassembled from the motor.

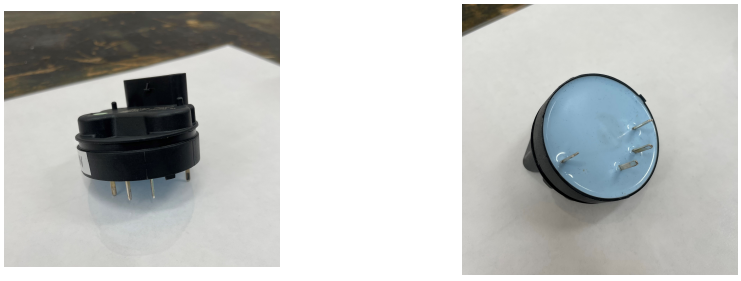

Figure 22: The ECU used for the motor control.

## 3.2 Software

The proposed methods are implemented in *Matlab/Simulink* and the C code is generated using *TargetLink/dSpace* software. To flash the code onto the ECU, an in-house software build tool provided by BorgWarner is used.

### 3.2.1 CANalyzer

To analyze the implementation and the behaviour of the motor both in real-time and post-testing, a software called *CANalyzer* from *Vector Informatik GmbH* is used. The license for this is provided by BorgWarner and is hardware based license as shown in figure 23.

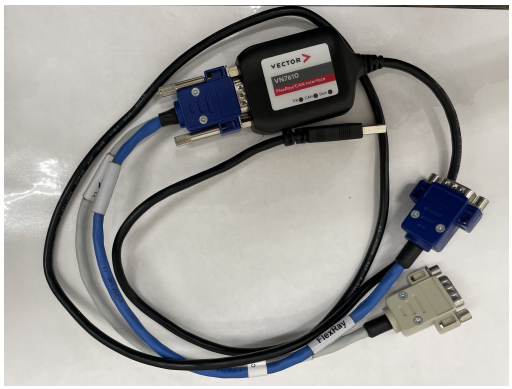


Figure 23: The CANalyzer hardware base license with *d-sub9* connectors for CAN and Flexray communication protocols. For this work only CAN protocol is used.

# 4 Method

This section provides an in-depth analysis of the implemented algorithm, explaining the rationale behind each step and measure taken to accomplish the desired goal. Additionally, it includes the presentation of analyzed data accompanied by insightful comments.

## 4.1 Implemented software

Two rotor position estimation methods have been implemented. From 0 $rad/s$ up to 50 $rad/s$, the high-frequency injection method is used and from 50 $rad/s$ up to the motor's top speed, the magnetic flux method is employed. To avoid unnecessary switching between the two methods, a hysteresis band has been implemented. Once the speed set point surpasses 50 $rad/s$, the flux-based method takes over. When decelerating, once the speed set point is set below 40 $rad/s$, the high-frequency method takes control.

The implemented software is divided in two main parts, namely, the high-frequency part and the part based on magnetic flux method. Further, the functionality of each of the blocks shown in the flowchart 24 are explained.

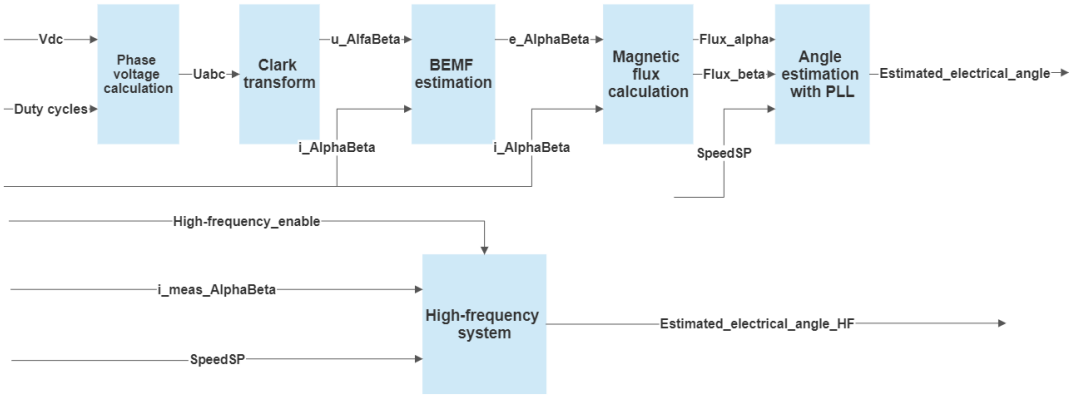


Figure 24: An overall flowchart of the implemented software. Note that there are different currents used in the BEMF estimation compared to the HF system. The HF system receives unprocessed measured currents, while the BEMF estimation receives the same currents as the current controller, which has the estimated high-frequency current responses removed.

## 4.2 Implementation of the magnetic flux based method

This section provides a detailed description of the measures taken in developing the rotor position estimation algorithm based on the estimated magnetic flux.

### 4.2.1 Phase voltage estimation

The implementation of the phase voltage estimation can be seen in figure 25. This is a simple estimation that omits the forward voltage drop in the transistors as well as the rise and fall time of the transistors.

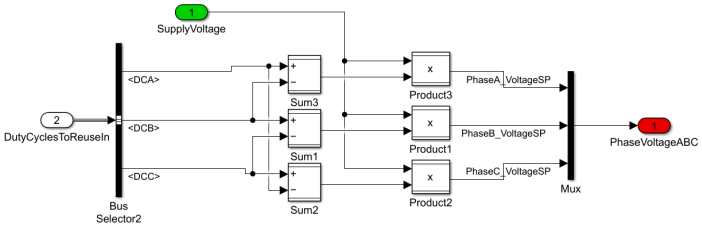


Figure 25: The calculation of phase voltages using the supply voltage and duty cycles.

In Equation 16, the mathematical description is provided. Here, $V_{cc}$ represents the supply voltage, while $DCA$, $DCB$, and $DCC$ denote the duty cycles for the three phases.

$$\begin{cases} V_A = V_{cc} \cdot (DCA - DCB) \\ V_B = V_{cc} \cdot (DCB - DCC) \\ V_B = V_{cc} \cdot (DCC - DCA) \end{cases} \tag{16}$$

### 4.2.2 The Clarke transform

Figure 26 shows the implementation of the Clarke transform of the estimated voltage.

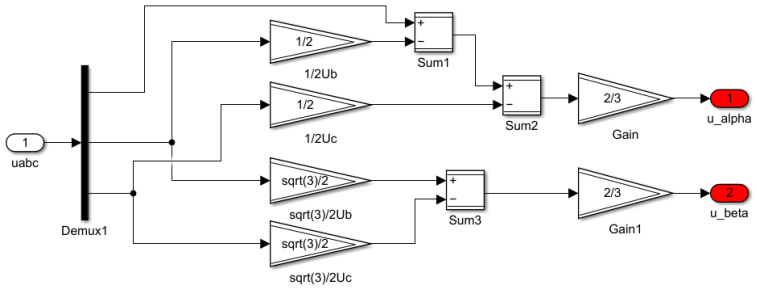


Figure 26: The calculation of $u_\alpha$ and $u_\beta$.

Equation 17 represents the calculation of $u_\alpha$ and $u_\beta$ shown in figure 26.

$$\begin{cases} u_\alpha = \frac{2}{3}\left(u_a - \frac{1}{2}u_b - \frac{1}{2}u_c\right) \\ u_\beta = \frac{2}{3}\left(\frac{\sqrt{3}}{2}u_b - \frac{\sqrt{3}}{2}u_c\right) \end{cases} \tag{17}$$

### 4.2.3 BEMF estimation

The implementation of the BEMF estimation is shown in figure 27.

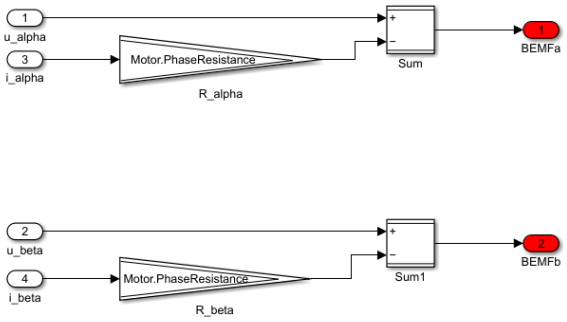


Figure 27: The calculation of the BEMF.

Since $i_\alpha$ and $i_\beta$ are measured signals, they may contain significant noise, as well as the nature of discrete time steps, the calculation of the current derivative is omitted. Equation 18 is used in the implementation of BEMF estimation shown in figure 27.

$$\overrightarrow{e} \approx \overrightarrow{v_{\alpha\beta}} - R \cdot \overrightarrow{i_{\alpha\beta}} \tag{18}$$

### 4.2.4 Magnetic flux calculation

Following the BEMF estimation, the next step is the implementation of the magnetic flux calculation, as shown in figure 28.

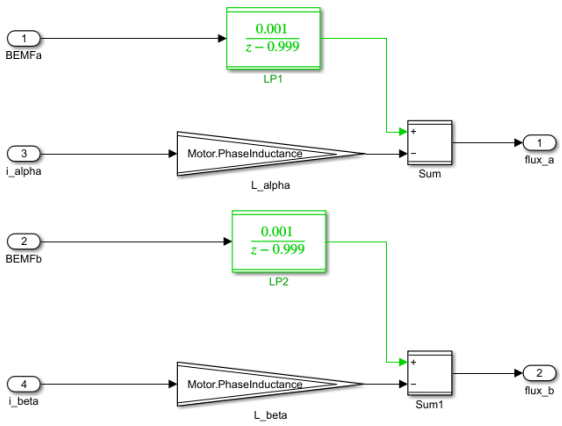


Figure 28: The calculation of the magnetic flux.

To integrate and extract the BEMF, an integrator along with a high-pass filter could be used. However, an alternative to that is to use a low-pass filter, as shown in equation 19.

$$\begin{aligned} \Psi_{s_{\alpha\beta}} &= H_{HP}\left(\int_0^t e_{\alpha\beta}\cdot dt\right) \approx H_{LP}\left(e_{\alpha\beta}\right) \\ H_{HP}\left(\int\left(e_{\alpha\beta}\cdot dt\right)\right) &= \frac{\tau s}{1+\tau s}\cdot\frac{1}{s}\cdot e_{\alpha\beta} \approx \frac{1}{1+\tau s}\cdot e_{\alpha\beta} = H_{LP}\left(e_{\alpha\beta}\right) \end{aligned} \tag{19}$$

where $H_{HP}$ is the transfer function of a high-pass filter, $H_{LP}$ is the transfer function of a low-pass filter, $\Psi_s$ is the stator flux and $e$ is the BEMF. Figure 28 shows the calculation of the magnetic flux as described in equation 7, but with an alternative approach to integration as shown equation 19.

The final step in calculating the magnetic flux $\overrightarrow{\Psi}_m$, as illustrated in figure 6, a calculation according to equation 20 is performed.

$$\overrightarrow{\Psi}_m = \overrightarrow{\Psi}_s - i_s \cdot L \tag{20}$$

### 4.2.5 Angle estimation with PLL

An overview of the angle estimation based on the calculated magnetic flux can be seen in figure 29.

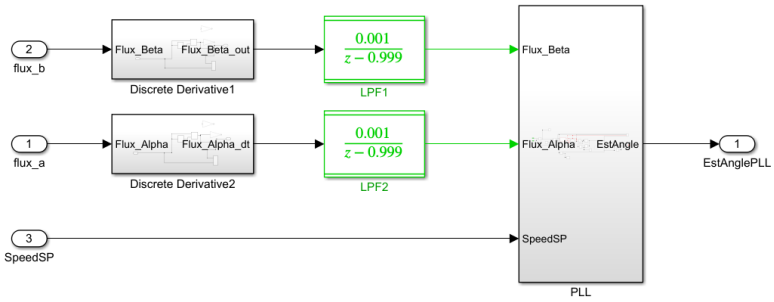


Figure 29: The overview of the rotor angle estimation implementation based on calculated magnetic flux.

The discrete derivative blocks are used to reduce the offset between $i_\alpha$ and $i_\beta$. This issue originates from the measured phase currents $U, V$ and $W$. As figure 30 illustrates, there is an offset in the measured phase currents.

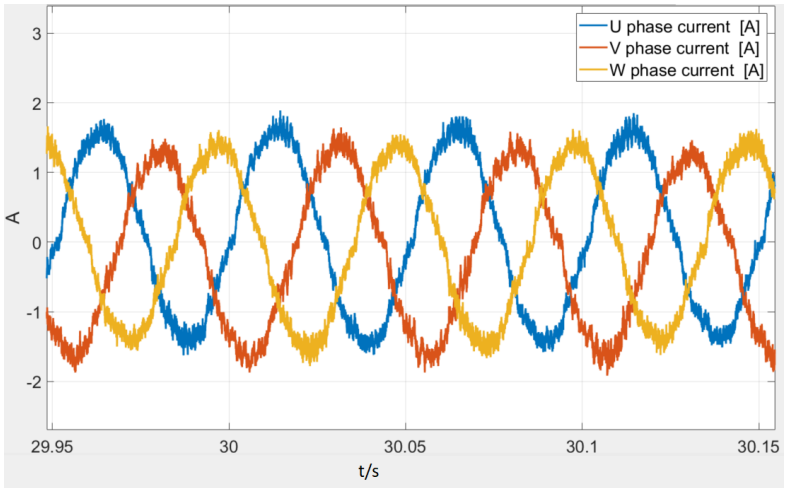


Figure 30: A plot of the measured phase currents $U, V$ and $W$. The x-axis represents time [s].

The offset issue demonstrated in figure 30 is apparent in the calculated magnetic flux, as can be seen in the left plot in figure 31. To resolve this issue, discrete derivative blocks are introduced. After applying the discrete derivative blocks, the signals in the right plot in figure 30 no longer exhibit the offset. It is important to note that the derivative operation phase shifts both signals by $\frac{\pi}{2}$, however, the LPF1 and LPF2 that follow after the derivative blocks, phase shifts those signals back by -$\frac{\pi}{2}$.

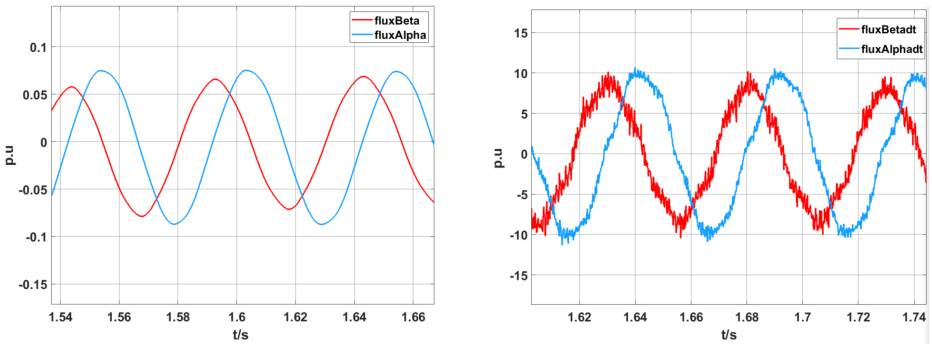


Figure 31: The observed offset between $\Psi_\alpha$ and $\Psi_\beta$ (left). However, after applying the discrete derivative, $\Psi_\alpha$ and $\Psi_\beta$ no longer exhibit the offset (right).

Without the discrete derivative blocks, the calculated angle would be unreliable, as shown in figure 32.

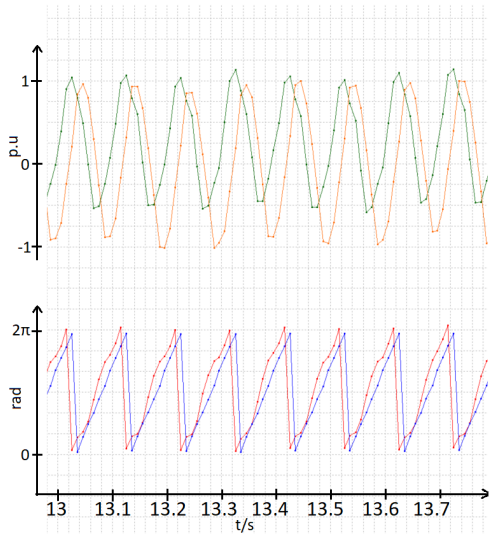


Figure 32: The observed offset between $\Psi_\alpha$ and $\Psi_\beta$ results in a fluctuating estimated rotor angle (red) observed in real-time using CANalyzer.

During testing, an unwanted common phase signal became apparent, as can be seen in the current and voltage waveforms in figure 33. This phenomenon is also reflected in the calculated magnetic flux in figure 34. To eliminate the low-frequency noise signal originating from measured currents and calculated phase voltages, as illustrated in figure 33, the PLL block is employed. Instead, it tracks a single-phase noise-free signal and estimates the rotor angle.

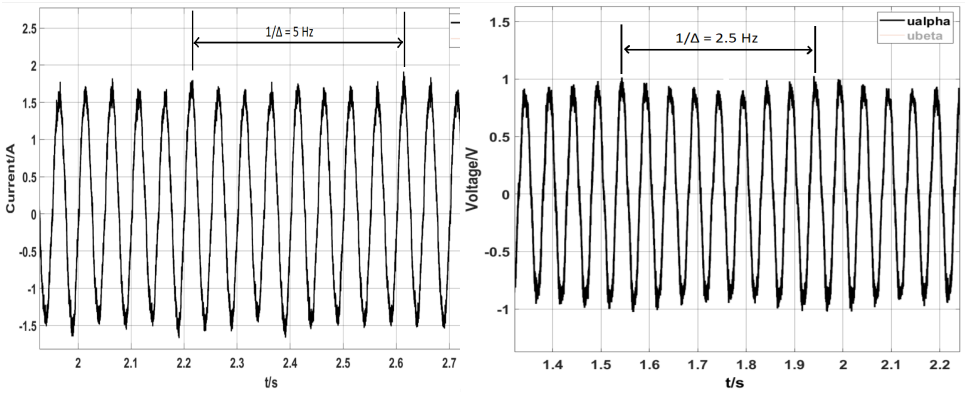


Figure 33: The measured current $i_\alpha$ (left) exhibits a 5Hz noise signal while the phase voltage $u_\alpha$ (right) shows a 2.5Hz noise signal. The low frequency noise eventually propagates to BEMF and magnetic flux calculations resulting in an increase in magnitude.

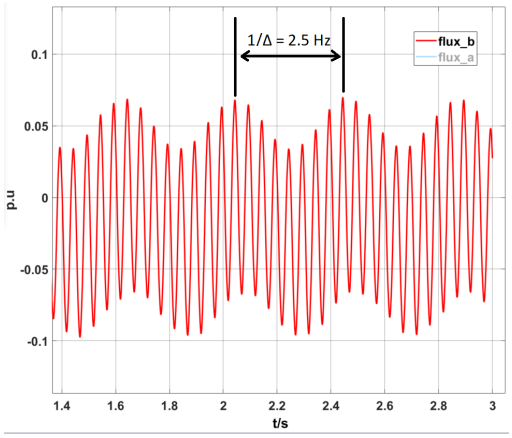


Figure 34: The calculated magnetic flux $\Psi_\beta$ exhibits a 2.5Hz noise signal, which can result in unreliable angle estimation. To address this issue, a phase-locked loop algorithm is used to track a single signal and estimate the rotor position based on that.

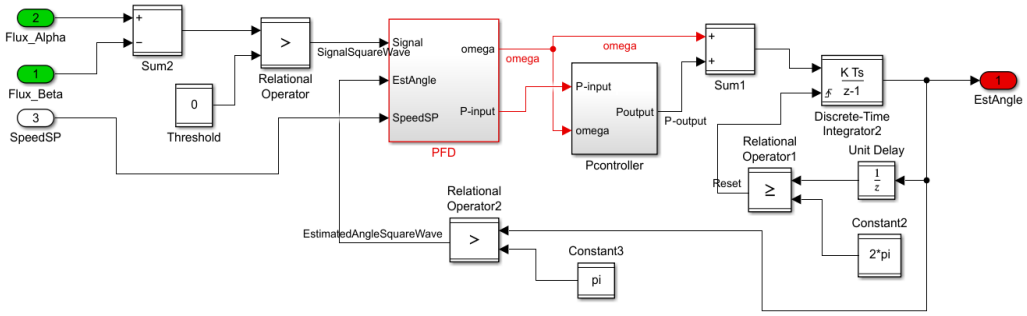


Figure 35: Detailed overview of the PLL system shown in figure 11. This system implements the PFD state machine described in figure 12.

The inputs to the PLL block in figure 35 are $\Psi_\alpha$ (`Flux_Alpha`), $\Psi_\beta$ (`Flux_Beta`) and the `SpeedSP`. Initially, the `Flux_Beta` is subtracted from `Flux_Alpha` to eliminate the low-frequency noise signal shown in figure 34. This is possible because the low-frequency noise signal present in both signals is a common phase signal, and subtracting them effectively cancels out the noise component.

The result from the subtraction is then passed into the PFD block as a square wave. The PFD detects the rising and falling edges of the square wave and based on the edge detections, calculates an input value (1, 0 or -1), as

described in figure 12, for the P-controller. The PFD also calculates $\omega_e$ based on the frequency of the square wave. The `SpeedSP` in PFD is used to switch between medium speed and high speed logic, depending on the speed set point. Both outputs from the PFD block serve as inputs to the P-controller.

Lastly, the outputs from the P-controller and $\omega_e$ are summed and integrated to obtain the estimated angle, which ranges from 0 and $2\pi$ radians. *Appendix A* provides a more detailed overview of the PFD implementation.

## 4.3 Implementation of high-frequency based rotor position estimation

The implementation of high-frequency based rotor position estimation involves generating a 416.67 Hz signal by creating 24 voltage vector set points during one electric period. These vectors are spaced at angles of 15° from each other.

To inject the high-frequency voltage into the motor, the resulting currents need to be subtracted from the measured current before being sent to the FOC current controller. This subtraction process aims to hide the high-frequency injection from the current controller. If the high-frequency current response is not hidden from the current controller, both the high-frequency current's amplitude and phase will be changed when passing through the controller, as shown in Figure 36.

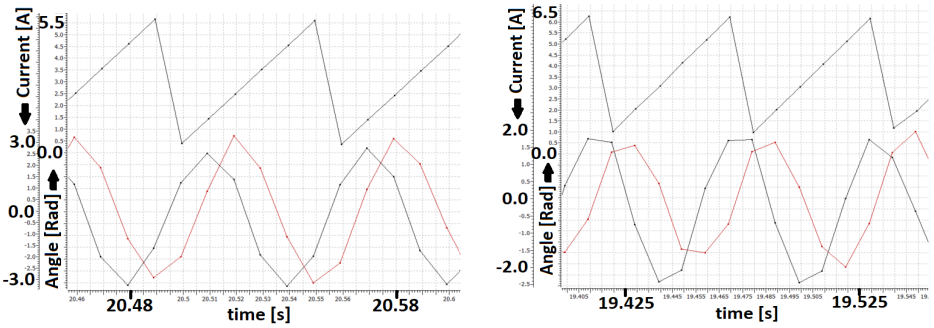


Figure 36: The left plot illustrates the high-frequency current response from a 1 $V_p$ HF voltage injection when the FOC current controller is disconnected. On the right plot, the high-frequent current response is displayed with the current controller connected. The top part of the figure represents the angle of the HF injection, while the bottom part of the figure presents the $\alpha\beta$ high-frequency current responses. Note that the signals shown in these plots experience aliasing due to sampling frequency of 100 Hz and signal frequency of 416.67 Hz.

If the subtraction of the resulting injection current is not hidden from the current controller, several problems can occur. Firstly, the FOC current controller will significantly alter and dampen the injection, rendering it unusable. Secondly, BorgWarner-specific safety features may be activated when the current does

not behave as expected, causing interruptions in the FOC current controller. Therefore, an additional current calculation, involving *InjectionCurrAlpha* and *InjectionCurrBeta*, is necessary to account for these issues, as depicted in Figure 37, is needed.

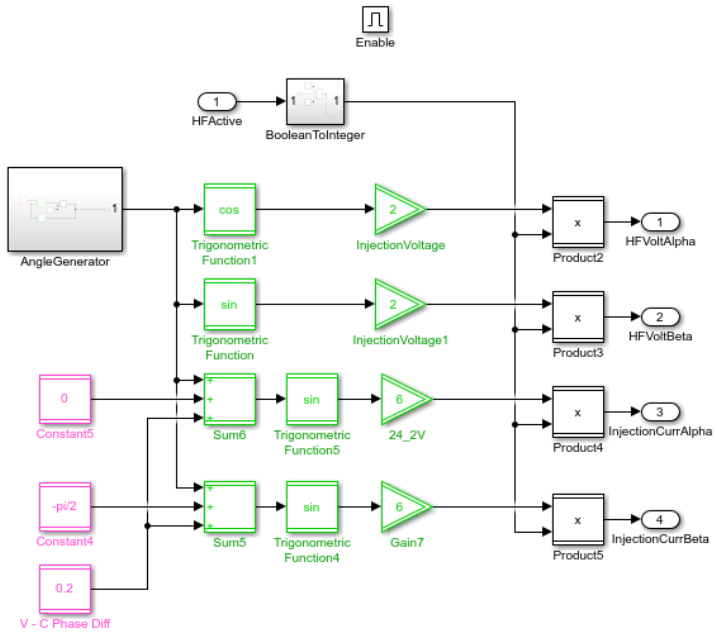


Figure 37: This figure shows the generation of HF voltage signals as well as the estimated high-frequency current response from the voltage injection.

The *Angle Generator* generates an angle slope that corresponds to a 416.67 Hz signal after passing through sinusoidal functions. The measurements of the current response to the given 2 $V$ high-frequency injection showed an amplitude of 6 $A$ and a phase lag of $(\frac{\pi}{2} - 0.2)$ radians when measured at standstill without the current controller connected. Equation 21 shows the mathematical representation of the implementation in figure 37.

$$\begin{cases} V_{HF_\alpha}(n) = 2 \cdot \cos(2 \cdot \pi \cdot \frac{1}{24} \cdot n) \\ V_{HF_\beta}(n) = 2 \cdot \sin(2 \cdot \pi \cdot \frac{1}{24} \cdot n) \\ I_{HF_\alpha}(n) = 6 \cdot \sin(2 \cdot \pi \cdot \frac{1}{24} \cdot n + 0.2) \\ I_{HF_\beta}(n) = 6 \cdot \sin(2 \cdot \pi \cdot \frac{1}{24} \cdot n + 0.2 - \frac{\pi}{2}) \end{cases} \tag{21}$$

The calculated high-frequency currents ($I_{HF_\alpha}$ and $I_{HF_\beta}$ in equation 21) are sub-

tracted from the measured currents before passed to the FOC current controller. It is important to note that the constants used in the high-frequency current estimation are determined empirically. While these constants may appear suitable for BLDC motors with identical design characteristics, their applicability might lead to a sub-optimal result. Therefore, it is recommended to test and verify these constants for a specific motor.

The high-frequency voltage set points are then passed to the FOC current controller and added in the *Inverse Park* calculation block, where the final $\alpha$ and $\beta$ voltage set points are determined. This can be seen in figure 38.

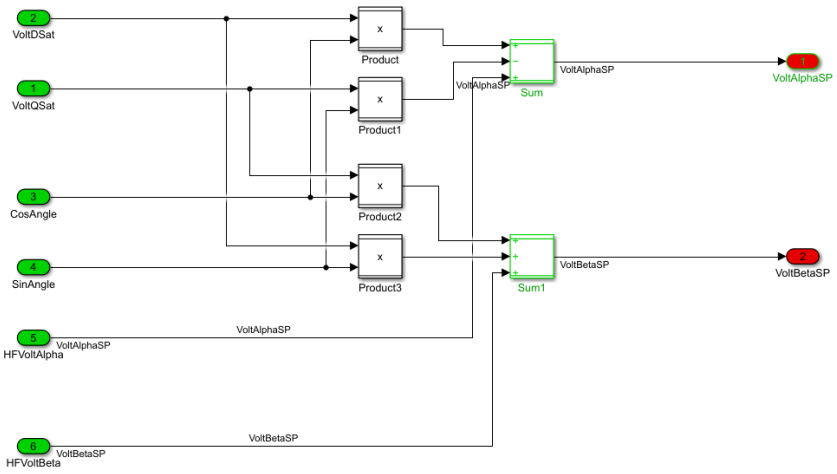


Figure 38: The final step in the FOC current controller where the alpha and beta voltage set points are calculated. Here, the high-frequency voltage vectors are added.

Equation 22 shows the mathematical representation of the implementation in figure 38.

$$\begin{cases} V_\alpha^* = V_{D_{Sat}} \cdot cos(\theta_r) - V_{Q_{Sat}} \cdot sin(\theta_r) + V_{HF_\alpha} \\ V_\beta^* = V_{Q_{Sat}} \cdot cos(\theta_r) + V_{D_{Sat}} \cdot sin(\theta_r) + V_{HF_\beta} \end{cases} \tag{22}$$

where $V_\alpha^*$ and $V_\beta^*$ are the $\alpha\beta$-voltage set points, $V_{D_{Sat}}$ and $V_{Q_{Sat}}$ are the voltage set points in the dq-plane, $\theta_r$ is the rotor angle, $V_{HF_\alpha}$ and $V_{HF_\beta}$ are the injected high-frequency voltage vectors.

It should be noted that the high-frequency voltage injection reduces the available voltage that can be used to generate useful driving torque in the motor. Additionally, it reduces the available current that contributes to the creation of useful driving torque, due to the current limit implemented in the system.

The overall implementation of the high-frequency injection rotor position estimation method is shown in figure 39.

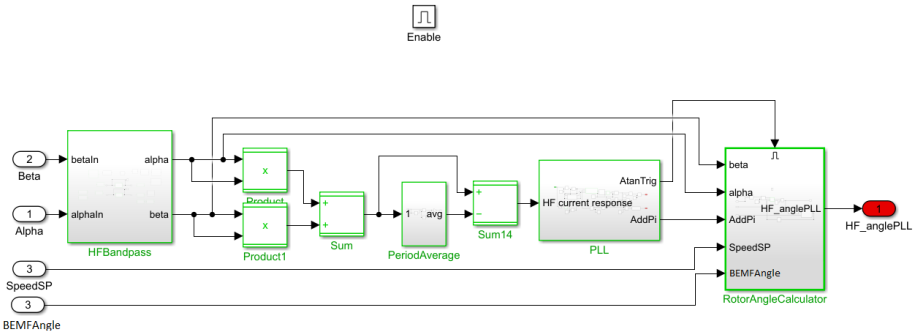


Figure 39: This figure shows the overall implementation of the high-frequency injection method for the rotor position estimation.

The $\alpha$ and $\beta$ high-frequency currents undergo several processing steps before the PLL can track the phase of the signal. First, they are passed through a band-pass filter that allows the high-frequency injection to pass through. Then, the square of the $\alpha$ and $\beta$ high-frequency currents is calculated and added together. Finally, the mean value from the last period is subtracted from the result, as shown in equation 23.

The PLL tracks the phase of the high-frequency current deviations caused by the difference in reluctance between the d and q axis, as illustrated in figure 10. At a certain angle ($\frac{3\pi}{2}$ radians), where the peak of the signal is expected, the logic triggers the last block, the *Rotor Angle Calculator*, to calculate the rotor angle.

$$\begin{aligned} &\begin{cases} i_{\alpha_{BP}} = H_{BPF}(i_\alpha) \\ i_{\beta_{BP}} = H_{BPF}(i_\beta) \end{cases} \\ &i_{sq} = i_{\alpha_{BP}}^2 + i_{\beta_{BP}}^2 \\ &i_{sq_{ac}} = i_{sq} - i_{sq_{dc}} \\ &i_{sq_{dc}} = \frac{1}{24} \sum_{i=n-23}^{n} i_{sq}(i) \end{aligned} \tag{23}$$

However, observing the processed current $i_{sq_{ac}}$ entering the PLL one distinct problem was found, namely, the difference between d- and q-current response from the voltage injection is not consistent. It appears to depend on several factors, primarily on the rotor position and omega, but also on the applied load on the motor. Figure 40 demonstrates this phenomenon.

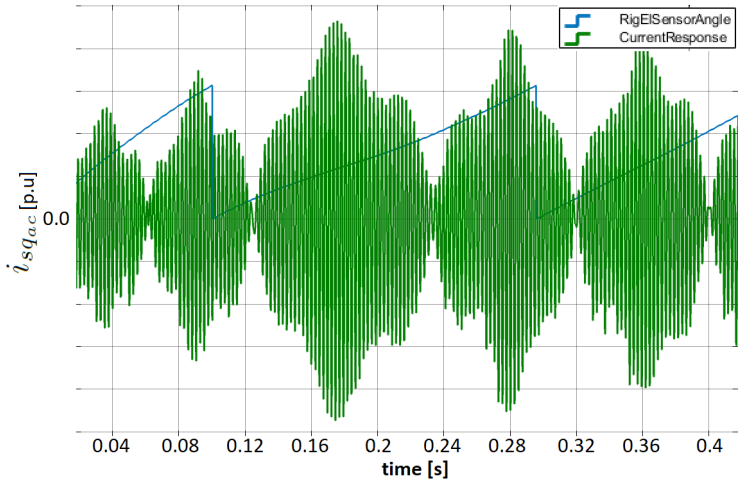


Figure 40: This figure shows the processed high-frequency current response $i_{sq_{ac}}$ and the electrical angle of the rig (not in phase with rotor angle), unlike the expected high-frequency current response this figure shows that the amplitude is not constant.

Furthermore, the high-frequency current response does not remain trustworthy when the amplitude from $i_{sq_{ac}}$ is low, in figure 41 this can be observed.

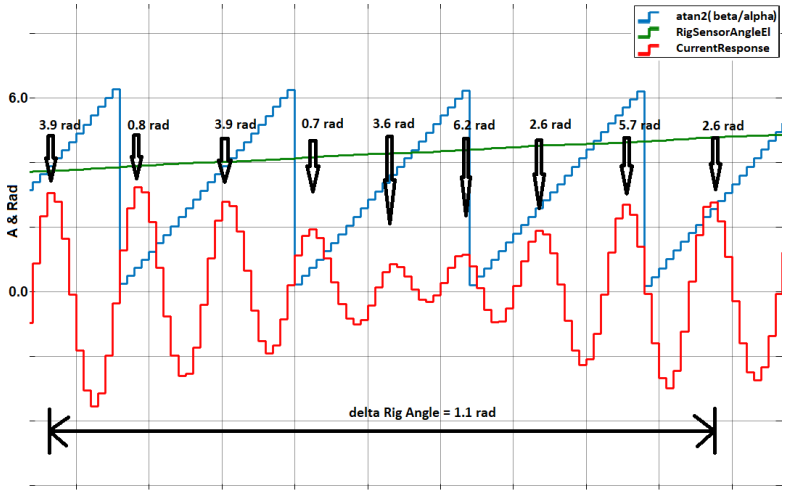


Figure 41: This figure shows the processed high-frequency current response $i_{sq_{ac}}$ and the electrical angle of the rig.

As seen in figure 10 in the theory, every other peak should correspond to the rotor +/- d-axis, and the angle should change by approximately $\pi$ radians between each peak. However, in this figure, it can be observed that the peaks of the high-frequency current response slip by approximately $\pi$ radians over several injection cycles when the amplitude of the signal decreases to a minimum.

This caused a major problem when trying to estimate the angle reliably, an attempt to resolve this problem was made in the HF PLL. However, the problem still remained at higher load cases.

The next step in calculating the rotor position addresses this issue by using a PLL. A detailed figure of the HF PLL is shown in the figure 42.

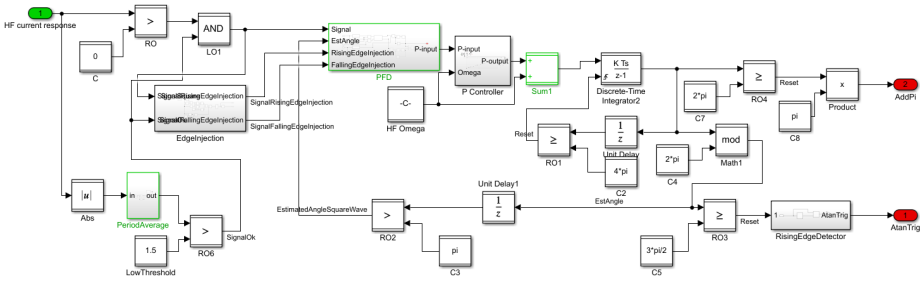


Figure 42: This figure shows the implementation of the HF PLL.

The HF PLL differs from the PLL employed in the flux observer in figure 35. Firstly, the HF PLL is not used to estimate the angle of the rotor but rather the angle of the high-frequency current response. It sends out a trigger to the next block when the $\alpha$ and $\beta$ high-frequency currents align with the rotor position.

Secondly, it keeps track of the phase of the signal from 0 to $4\pi$ radians, this is because the signal input into the PLL consists of two periods during one injection period, as explained in section 2.4.

Finally, the HF PLL must handle the phase shift in the high-frequency current peaks that occurs when the amplitude of the $i_{sq_{ac}}$ signal becomes too low. To address this issue, an additional filter is introduced to modify the input seen by the phase frequency detector (PFD). This filter eliminates unreliable data points and generates extra edges in the input signal for the PFD, estimating their positions. The estimation of these edges follows a specific procedure: a counter continuously counts discrete time steps and triggers an edge when it reaches 12 (this is half of the 24 discrete time steps of one HF period), provided that the input signal's amplitude is low. However, this counter is reset each time a reliable edge or an injected edge is detected. Additionally, if a reliable edge appears relatively close to the last injected edge, it is removed to prevent disturbances in the PLL's stability.

The final step in the high-frequency rotor position estimation is the calculation of the rotor position, which is triggered by the HF PLL. The implementation of this step can be seen in figure 43.

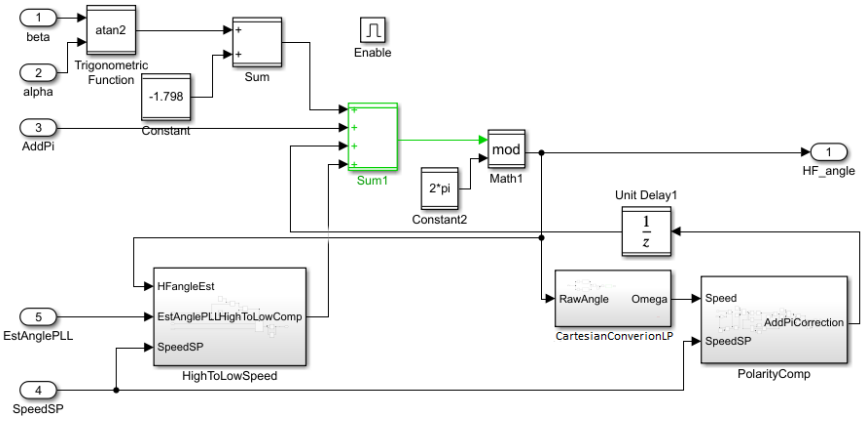


Figure 43: This figure shows the implementation of the final step when calculating the rotor position. A more detailed implementation of "HighToLowSpeed", "CartesianConvertionLP" and "PolarityComp" can be seen in appendix A.

The rotor position is determined by using an *arctan2* function to calculate the angle of the high-frequency current response in $\alpha$-$\beta$ coordinates. This angle can then be converted to the rotor position by subtracting an empirically determined constant 1.798 rad/s, namely, $\frac{\pi}{2}$ to align the angle with the q axis, which is used as a reference in the FOC current controller, and finally $C = 0.227$ is subtracted to approximately match the sensor angle during no load conditions.

In addition to calculating the angle to the d axis, this block also detects if the PLL has locked onto the wrong phase, by doing this it can estimate the rotor position. The detection of the wrong phase lock is handled in two separate ways. The first way is by observing the speed response of the motor compared to the speed set point. If the estimated angle deviates by $\pi$ from the true angle, the torque response will be negative, causing the rotor to spin in the opposite direction when a speed set point is activated. By applying a low-pass filter to the angle estimation it is possible to extract the speed, without the low-passed angle estimation the speed would be far to noisy.

The angle can not be filtered directly due to the fact that it exhibits discontinuity. To solve this, *Polar to Cartesian* coordinate conversion is necessary. The differences between applying a low-pass filter to the angle directly versus to the in-phase and quadrature components can be seen in figure 44.

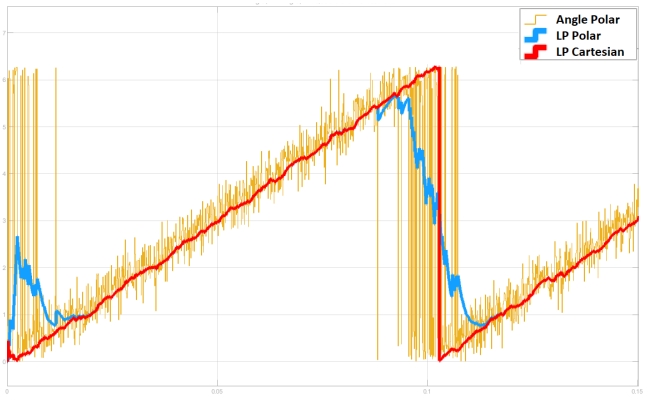


Figure 44: This figure shows the estimated raw polar angle (orange), low-passed Polar angle (blue) and the low-passed Cartesian angle (red).

The second way to detect if the PLL has locked onto the wrong phase is by comparing the angle estimation to the flux observer's angle estimation. During deceleration, while transitioning from using the flux observer's angle estimation to using the high-frequency injection, there is a chance that the HF PLL locks onto the wrong phase. To determine this, the angles between the flux observer's angle estimation and the HF angle estimation are compared. If the difference between the two angles is approximately $\pi$, a correction is made by adding $\pi$ to the HF angle estimation. This comparison can only be made when both angle estimation methods are active and reliable, which is true when the speed set point is above 40 rad/s and below 50 rad/s. Above 50 rad/s, the high-frequency injection is not active.

# 5 Results

In this section, we present the results of the rotor angle estimation using high-frequency and flux observer methods, and compare them to the sensored implementation.

Firstly, we provide real-time plots that illustrate the relationship between the sensor angle and the estimated angle obtained through both methods. These plots offer a visual comparison of the accuracy and effectiveness of the rotor angle estimation techniques, additionally, transitions between the two estimation methods are shown.

Secondly, we conduct a performance comparison between the implemented sensorless FOC and sensored FOC by analyzing the maximum measured torque the motor can hold at different speeds.

To gain a deeper understanding of the angle at which the BLDC motor applies its current, we present plots of the d-q currents for both the sensorless FOC and sensored FOC. Additionally, we estimate the angle error based on the d-q current plots, providing a quantitative measure of the accuracy and precision of the rotor angle estimation methods applied.

Lastly, we present plots that illustrate the $\alpha\beta$-current responses resulting from the high-frequency injection.

Note that in the plots 45 to 49 the signals are sampled at 100 Hz, which leads to aliasing and is especially noticeable at high speeds.

## 5.1 Rotor angle estimation using the high-frequency injection method

Figures 45 to 49 illustrate the performance of the HF injection angle estimation method.

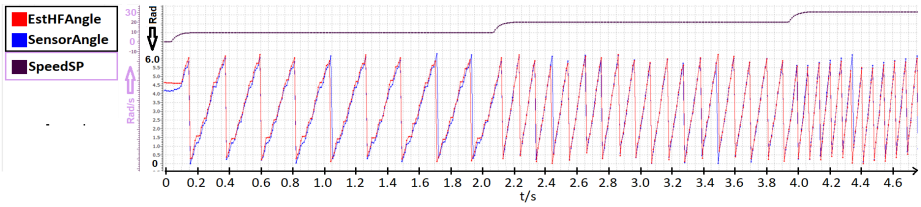


Figure 45: Real-time plot comparing the HF estimated angle with the electrical sensor angle from standstill up to $\omega_m = 30$ rad/s under no-load conditions.

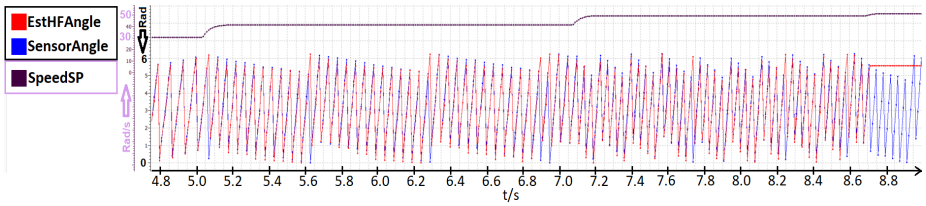


Figure 46: Real-time plot comparing the HF estimated angle with the electrical sensor angle from $\omega_m = 30$ rad/s up to $\omega_m = 50$ rad/s under no-load conditions. At $\omega_m = 50$ rad/s the HF injection is disabled. Note that the visible low frequency noise in the angle signals are due to aliasing.

## 5.2 Rotor angle estimation using the magnetic flux method

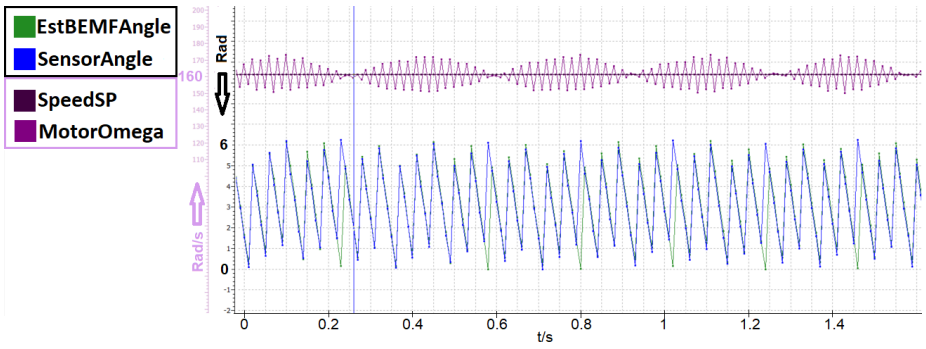


Figure 47: Real-time plot comparing the estimated angle using the magnetic flux method with the electrical sensor angle at $\omega_m = 160$ rad/s under no-load conditions. Note that the rotor still spins in a positive direction even though it appears to be spinning in the opposite direction. This is due to aliasing.

## 5.3 Transition between the two estimation methods

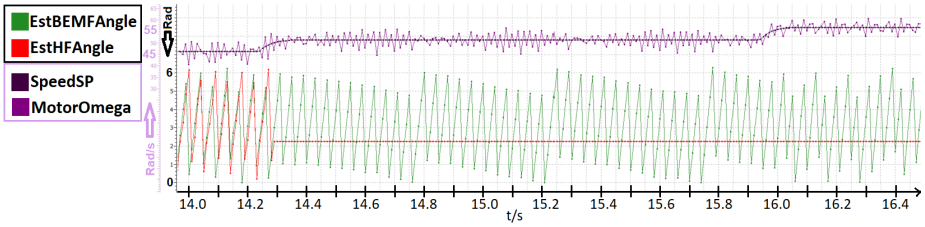


Figure 48: Real-time plot illustrating the transition from using the HF estimated angle control to using the estimated angle from the magnetic flux method. The transition occurs at $\omega_m = 50$ rad/s. The plot also includes the speed set point and the measured speed, demonstrating the smooth transition and the motor's ability to maintain the speed set point. Note that the visible low frequency noise in the angle signals are due to aliasing.

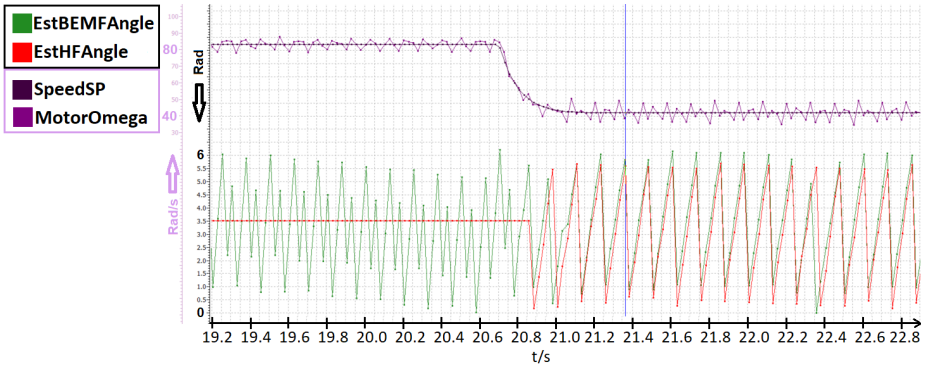


Figure 49: Real-time plot demonstrating the transition from using the estimated angle control from the magnetic flux method to using the HF estimated angle method. A step change in speed set point is made from $\omega_m = 80$ rad/s to $\omega_m = 40$ rad/s, with the transition occurring at $\omega_m = 50$ rad/s. The plot includes the speed set point and the measured speed, illustrating the smooth transition and the motor's ability to maintain the speed set point.

## 5.4 Torque and speed performance

The performance limit in terms of torque ($Ncm$), comparing the original sensored FOC control with the sensorless FOC is illustrated in figure 50.

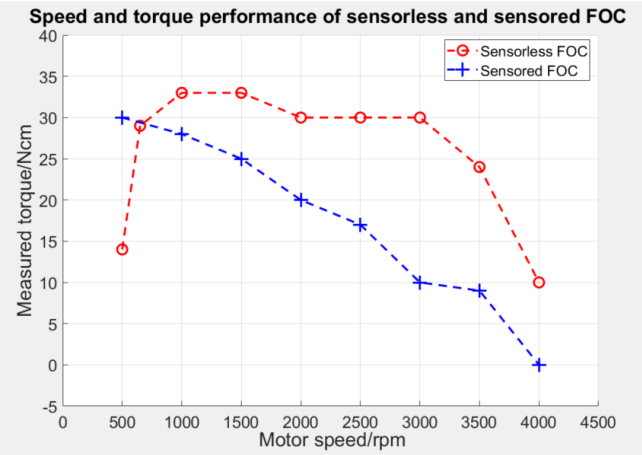


Figure 50: Performance comparison of sensored FOC and sensorless FOC from 500 rpm up to 4000 rpm with load torque applied until the breaking point. The breaking point in terms of torque is plotted on the Y-axis of the graph.

## 5.5 Direct and quadrature currents

To gain a better understanding of the behaviour of the BLDC motor with the sensorless FOC control implementation, it is crucial to examine the direct and quadrature currents. These currents provide insights into the angle at which the FOC controller operates since it only sets the q-current and keeps the d-current set to zero in the dq-frame. The plots of d-q currents for sensored FOC and sensorless FOC at different speeds and loads are presented, allowing a comprehensive analysis.

### 5.5.1 Plots of the direct and quadrature currents

Figures 51 to 59 illustrate the d-q current plots.

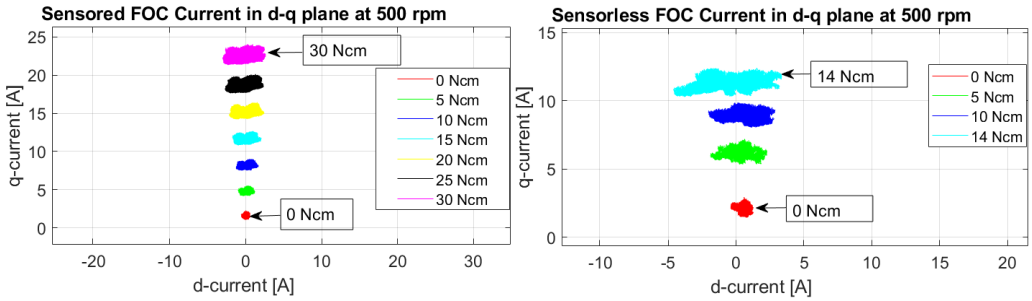


Figure 51: The behaviour of the dq-currents at constant speed of 500 mechanical rpm with different loads, the highest load case achieved by sensored FOC was 30 Ncm while the sensorless FOC achieved 14 Ncm.

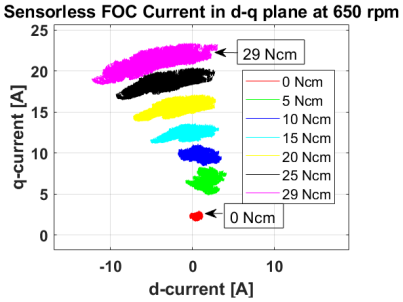


Figure 52: The behaviour of the dq-currents at constant speed of 650 mechanical rpm with different loads, the highest load case achieved by the sensorless FOC was 29 Ncm.

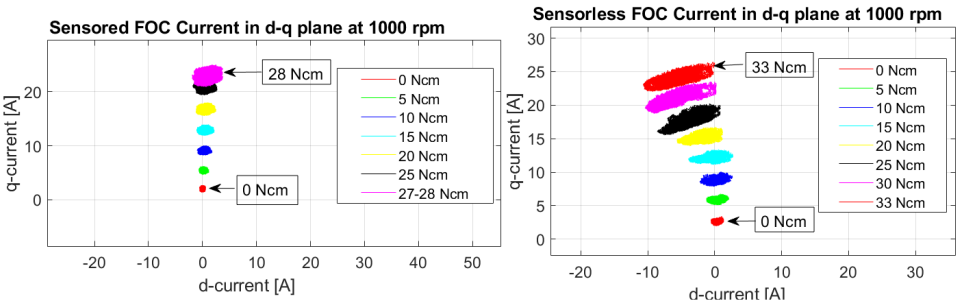


Figure 53: The behaviour of the dq-currents at constant speed of 1000 mechanical rpm with different loads, the highest load case achieved by sensored FOC was 28 Ncm while the sensorless FOC achieved 33 Ncm.

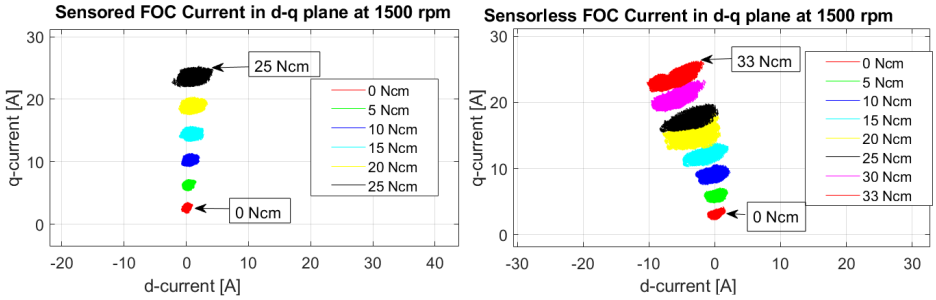


Figure 54: The behaviour of the dq-currents at constant speed of 1500 mechanical rpm with different loads, the highest load case achieved by sensored FOC was 25 Ncm while the sensorless FOC achieved 33 Ncm.

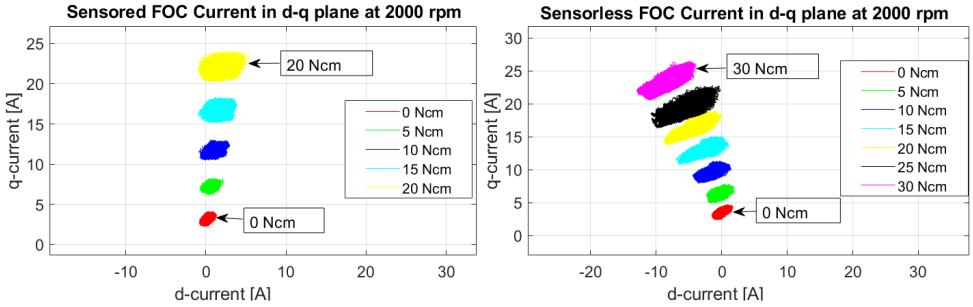


Figure 55: The behaviour of the dq-currents at constant speed of 2000 mechanical rpm with different loads, the highest load case achieved by sensored FOC was 20 Ncm while the sensorless FOC achieved 30 Ncm.

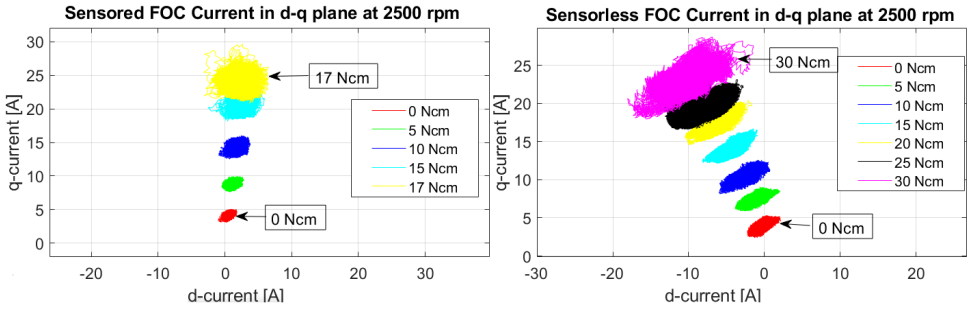


Figure 56: The behaviour of the dq-currents at constant speed of 2500 mechanical rpm with different loads, the highest load case achieved by sensored FOC was 17 Ncm while the sensorless FOC achieved 30 Ncm.

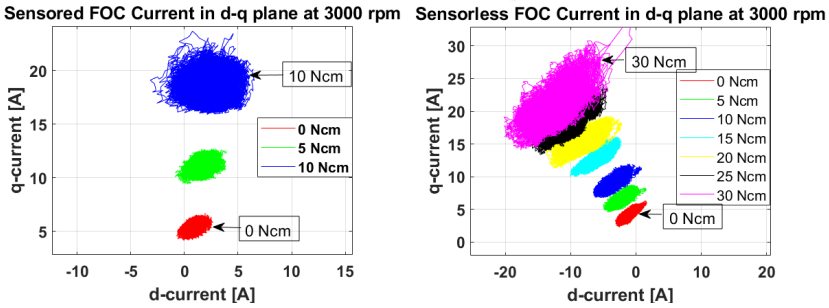


Figure 57: The behaviour of the dq-currents at constant speed of 3000 mechanical rpm with different loads, the highest load case achieved by sensored FOC was 10 Ncm while the sensorless FOC achieved 30 Ncm.

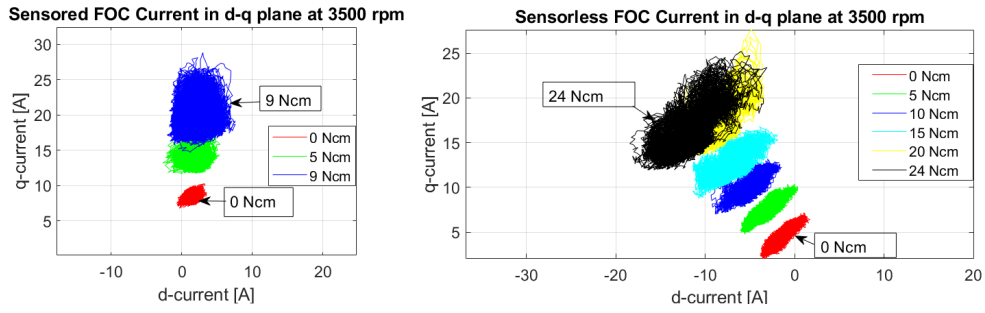


Figure 58: The behaviour of the dq-currents at constant speed of 3500 mechanical rpm with different loads, the highest load case achieved by sensored FOC was 9 Ncm while the sensorless FOC achieved 24 Ncm.

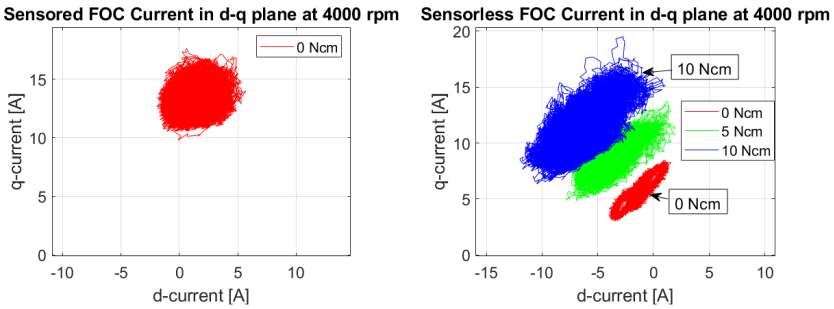


Figure 59: The behaviour of the dq-currents at constant speed of 4000 mechanical rpm with different loads, the highest load case achieved by sensored FOC was 0 Ncm while the sensorless FOC achieved 10 Ncm.

### 5.5.2 Estimated angle based on d-q plots

By analyzing the d-q current plots, the angle estimation error can be extracted. The average values from the d-q current reveal that the angle estimation error varies from -15.18° at low speed and low torque to +27.38° during high speed and high load conditions. Due to this error the torque performance was increased as seen in figure 50. Figure 60 illustrates the error of the angle estimation based on the dq-currents.

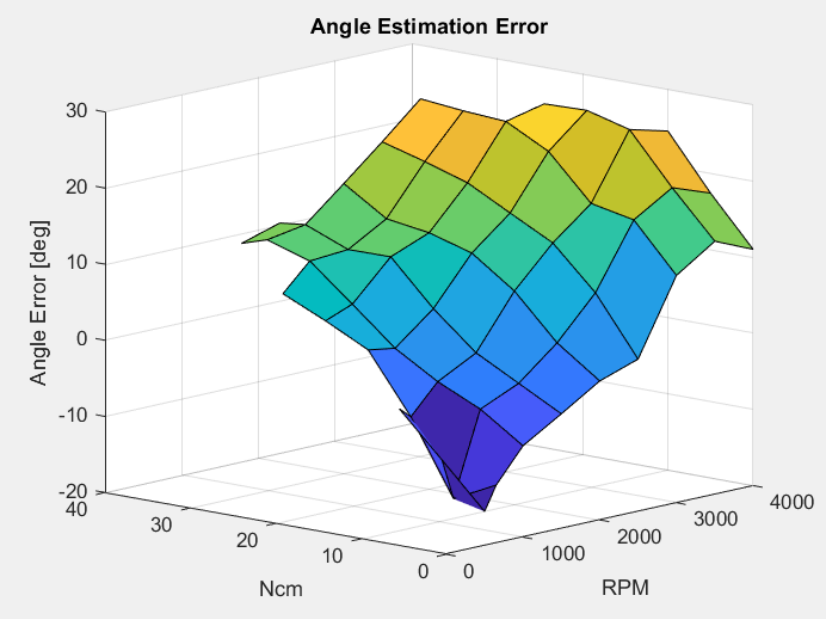


Figure 60: The angle estimation error based on the d-q currents.

## 5.6 High-frequency current response

The HF current response is shown in figure 61. The left graph illustrates the current response in $\alpha\beta$-plane. As explained in theory (figure 10), an ellipse is observed. However, the graph on the right shows that the current response appears to be circular. This phenomenon is discussed in figure 40.

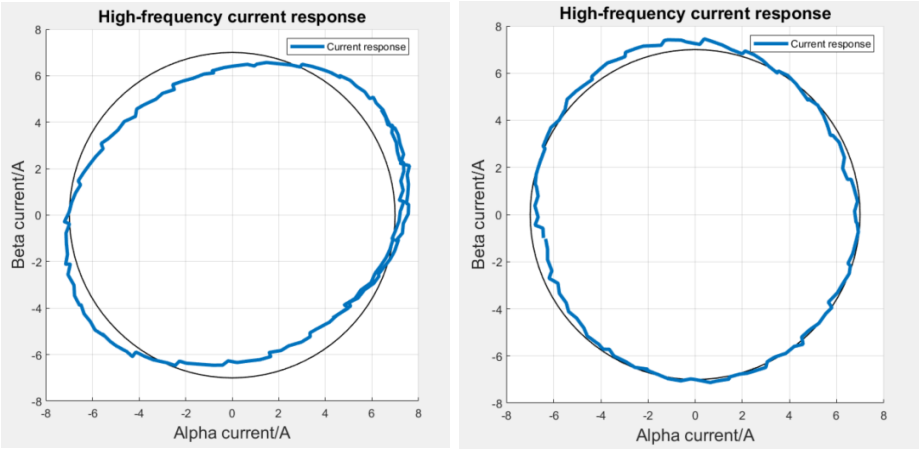


Figure 61: The current response in $\alpha\beta$-plane while high-frequency injection is active. The black circle in both figures serves as a visual reference. There is no difference in motor operation between the left and right plots shown in this figure. The left plot illustrates the high-frequency current response when the amplitude is at its highest, while the right plot illustrates the high-frequency current response with a very low amplitude. Referring to Figure 40, the left plot corresponds to $t = 0.28$ s and the right plot corresponds to $t = 0.32$ s.

# 6 Discussion

This section provides a discussion of the results obtained from the implemented rotor angle estimation methods. We examine the strengths, weaknesses, advantages, and limitations of each method, shedding light on their performance and applicability in practice. Additionally, we highlight the challenges that arose during the implementation process and discuss the solutions that were developed to overcome them. Lastly, a few comments on the implementation process itself are given.

## 6.1 BEMF-based methods

In this section, we discuss two different angle estimation methods based on back electromotive force at medium and high speeds.

### 6.1.1 The two-argument arctangent method

The first implemented method was the two-argument arctangent method, which aimed to calculate the rotor angle based on the $\alpha$ and $\beta$ components of BEMF. Initially, the proof of concept for this method was demonstrated successfully under no-load conditions. However, as the speed increased and the motor operated under load, several issues were encountered that rendered this method ineffective.

One significant challenge was the presence of low-frequency noise signals, as depicted in figure 33. These noise signals introduced disturbances in the BEMF measurements, leading to inaccuracies in the estimated rotor angle. Additionally, another problem arose from the offset in phase currents, as shown in figure 32. This offset affected the accuracy of the estimated angle obtained from the two-argument arctangent method.

Consequently, the estimated rotor angle derived from the *atan2* method became unreliable and unsuitable for the FOC implementation. Nevertheless, this method demonstrated the potential of using BEMF for rotor angle estimation. Further development is necessary to address the challenges associated with noise signals and offset issues to make this method viable for practical applications.

### 6.1.2 QPLL method

As an alternative to the *atan2* method, a Quadratic Phase-Locked Loop (QPLL) method was tested. Similar to the previous method, the QPLL method showed promise in estimating the rotor position accurately under no-load conditions. However, it faced similar challenges when a load was applied.

The QPLL method, like the *atan2* method, was affected by low-frequency noise signals and offset in phase currents, leading to inaccuracies in the estimated angle as the motor operated under load.

Further improvements are required to overcome the challenges associated with noise and offset issues for the QPLL method to be reliably used in practical

sensorless control applications. Addressing these limitations would enhance the accuracy and robustness of the rotor angle estimation, enabling its successful implementation in a wider range of operating conditions.

### 6.1.3 PLL method

The PLL method demonstrated excellent performance from 650 rpm up to 4000 rpm, exhibiting a robust ability to withstand high loads, as illustrated in figure 50. To achieve this level of performance, several signal processing techniques were employed.

Firstly, a low-pass filter with a very low cut-off frequency was applied to the BEMF signals, the aim was to reduce noise originating from the measured phase currents. Consequently, a signal in phase with the flux was acquired. This filtering step played a crucial role in improving the accuracy of the estimated rotor angle.

Secondly, the offset issue in the phase currents, as shown in figure 32, was successfully resolved by introducing discrete derivatives, as shown in figure 29. This adjustment played a crucial role in eliminating the offset while retaining a known phase, thereby significantly enhancing the accuracy of rotor angle estimation.

Furthermore, the common-mode low-frequency noise signal present in both $\alpha$ and $\beta$ signals, as observed in figure 34, was effectively eliminated using signal processing techniques, seen in figure 35. These noise reduction measures significantly contributed to the overall performance of the PLL method.

The successful performance of the PLL method highlights the critical importance of robust signal processing techniques in achieving accurate rotor angle estimation. The implemented signal processing steps, including low-pass filtering, offset elimination, and noise reduction, collectively contributed to the high performance and reliability of the PLL method.

One limitation of the current implementation of the PLL method is its inability to detect negative rotational direction. This is because the method relies on a single signal for tracking the rotor angle, unlike the QPLL method, which is capable of estimating the rotor angle in both positive and negative rotational directions. However, considering that the intended application for this implementation is a pump, which requires a positive rotational direction, the inability to detect negative rotation was not considered a problem. If bi-directional operation were to be required, slight modifications to the PLL algorithm could easily address this limitation.

In addition to the improved performance at high speeds, the sensorless FOC implementation also proved to enhance efficiency, as evident in the d-q plots. The leading rotor estimation played a crucial role in achieving both the efficiency and performance enhancement. It is worth noting that the leading estimation can be attributed to the omission of the stator current derivative calculation in equation 18. This simplification had a positive impact on the performance of the sensorless FOC system.

## 6.2 High-frequency method

The implementation of the high-frequency method exhibited poor performance under load conditions, as indicated by the phenomenon described in figure 40. However, during light loads and moderate speeds up to 600 rpm, the method performed well when the logic to handle the reduced high-frequency current response $i_{sq_{ac}}$ was active.

The underlying cause of this phenomenon has not been fully resolved, but several hypotheses can be ruled out, leading to a more likely explanation. One initial hypothesis suggested that the reluctance in the d and q axes became the same, resulting in identical high-frequency current responses. However, based on figure 21, where the inductances were plotted for various current positions, it is clear that the inductances never approached each other, even at currents up to 25 amperes. Therefore, this hypothesis is unlikely.

Another hypothesis considered the possibility that the waveform of the BEMF introduced a 6th-order overtone compared to the estimated sinusoidal BEMF used by the FOC current controller. This overtone could potentially significantly affect the length of the HF voltage vector during its cycle. However, when comparing the frequency of the HF injection to the 6th-order overtone of the BEMF at 100 mechanical rpm, where this phenomena was clearly visible, it was found that the overtone was approximately 14 times slower than the HF injection. Consequently, it can be considered as a DC voltage during one injection cycle, which should not significantly alter the shape of the $\alpha\beta$-ellipse, but rather introduce a DC offset to the center of the ellipse.

Through thorough analysis, the hypothesis with the highest likelihood of explaining the phenomenon is related to the simplification made in the calculated high-frequency current response, as shown in figure 37. This simplified high-frequency current response does not consider the change in high-frequency current amplitude based on the location of the voltage vector in correlation to the rotor position in the d-q plane. As a result, a portion of the high-frequency current response is passed on to the FOC current controller. Given that the current controller has previously demonstrated significant damping and alteration of the HF injection, it will also affect the portion of the high-frequency injection that passes through after the attempted subtraction from the FOC current controller partially failed. Essentially, this means that deviations in the current seen by the controller will occur, except for the exact rotor position for which the high-frequency current response divides equally across $\alpha$ and $\beta$. The controller will attempt to maintain a specific current set point, leading to the deviation being damped and reshaping the $\alpha\beta$-current ellipse into a circle, as shown in figure 61.

The observed deviation in the high-frequency current response caused by the interaction between the high-frequency injection and the FOC current controller, highlights the limitations of the high-frequency current subtraction approach in maintaining accurate control in the high-frequency method. Attempts were made to address this issue by introducing a Notch filter or subtracting the high-frequency band-passed current component. However, these attempts did not

show success. A potential solution could be subtracting the exact ellipsoidal $\alpha\beta$-current response generated by the high-frequency voltage injection from the current controller. Unfortunately, due to the time constraints, addressing this issue thoroughly was not possible. To achieve more precise control, further refinements are necessary to account for the effects of the FOC current controller on the HF injection and ensure a reliable estimation of the rotor position.

## 6.3 Hardware and previously implemented software

The implementation of the project was carried out using *Simulink* in conjunction with *TargetLink* code generation, which imposed restrictions on the available blocks to those compatible with *TargetLink*. This significantly increased the implementation time as several complex *Simulink* blocks such as FFT, discrete filters, and specialized controller blocks were inaccessible. Consequently, alternative approaches or the construction of these blocks had to be implemented.

Considerable time was dedicated to comprehending the behavior of the existing Speed and Current controllers. Both controllers showed highly aggressive characteristics, with the Current controller even canceling out the HF injection. To address this issue, the high-frequency current response estimation shown in figure 37 needed to be subtracted from the measured current before entering the Current controller.

Another challenge originated from the Speed controller, which introduced oscillations similar to those described in figure 34. For testing purposes, the aggressiveness of the Speed controller was reduced, resulting in improved behavior. However, it was preferred by BorgWarner to maintain the original design aggressiveness of the Speed controller, requiring alternative solutions to be explored.

There were several performance-related issues with the ECU. Firstly, the CPU load of the ECU consistently approached its limit when testing new unoptimized implementations, causing the ECU to reset when the algorithm involved too many calculations. One proposed solution was to decrease the sampling frequency of the FOC block from 10 kHz to 5 kHz, but implementing this adjustment proved to be challenging. Lastly, the bandwidth of the bandpass filter in the HF algorithm (figure 15) had to be widened beyond the theoretically optimal range. This compromise was necessitated by the occurrence of rounding errors in the ECU, which interfered with the proper functioning of the HF algorithm.

Despite these challenges, the implementation process provided valuable insights into the limitations and complexities associated with hardware constraints and pre-existing software. Overcoming these obstacles required resourcefulness and creative problem-solving, ultimately contributing to a more robust understanding of the system and its performance characteristics.

# 7 Conclusion and future work

This chapter concludes the findings of the implemented sensorless rotor position estimation methods and suggests future directions for improvement.

## 7.1 Conclusion

The best method for medium and high speed was the magnetic flux method with PLL implementation. The PLL method based on the magnetic flux estimation proved to be the most reliable and effective. The PLL method demonstrated a monotonic behavior and outperformed the sensored FOC above 650 rpm. The sensorless FOC could withstand more load than the sensored FOC at medium and high speeds. The sensorless FOC demonstrated higher load capacity. For instance, at 2000 rpm, the breaking point for the sensorless FOC occurring at 30 Ncm while for the sensored FOC at 20 Ncm.

The high-frequency injection method, based on the saliency characteristics, proved the ability to estimate the rotor position at standstill and low speeds up to 60 (mechanical) rad/s. However, it encountered limitations when a load was applied, leading to poor performance.

## 7.2 Future work

Future work should focus on optimizing the calculated high-frequency current response from the high-frequency voltage injection in the HF-based rotor estimation method. By fine-tuning the current response calculation, significant improvements in stability and performance can be achieved for high-frequency rotor position estimation.

# 8 References


Abo-Khalil, A.G., (2020). Sensorless rotor position estimation of PMSM for low and high rotor speed. Electrical Engineering Department, Majmaah University, Almajmaah 11952, Kingdom of Saudi Arabia. Electrical Engineering Department, Assiut University, Assiut, 71515, Egypt DOI: 10.36909/jer.v9i2.9693. https://kuwaitjournals.org/jer/index.php/JER/article/view/9693. Accessed on 2023-06-15.

Alaküla, M., Bängtsson, H., and Karlsson, P. (2019). Power Electronics Devices, Converters, Control and Applications., p 273, 298-299, 364-366.

Gieras, J.G., Wang, R., Kamper, M.J. (2008). Axis Flux Permanent Magnet Brushless Machines. 2nd edition. Springer. ISBN 978-1-4020-6993-2, p241.

O'Rourke, C.J., Qasim, M.M., Overlin, M.R., Kirtley, J.L. (2019). A Geometric Interpretation of Reference Frames and Transformations: dq0, Clarke, and Park. IEEE Transactions on Energy Conversion 34,4:2070 - 2083 © 2019 IEEE. DOI: 10.1109/TEC.2019.2941175. https://ieeexplore.ieee.org/document/8836094. Accessed on 2023-06-15.

Peilin, Xu. (2017). Novel Sensorless Control for Permanent Magnet Synchronous Machines Based on Carrier Signal Injection. Diss. Department of Electronic and Electrical Engineering. The University of Sheffield. https://etheses.whiterose.ac.uk/17617/. Accessed on 2023-05-23.

Rice, M. An Introduction to Discrete-Time Filter Design. Brigham Young University. http://ece390web.groups.et.byu.net/dokuwiki/lib/exe/fetch.php?media=filter_design_notes.pdf. Accessed on 2023-03-15.

Sang-Hoon, K. (2017). Electric Motor Control. DC, AC, and BLDC Motors. ISBN: 9780128121382. Elsevier., p169, 392.

Shujin, C., Baozhu, M., Zhengyun, R., Fei, G., Huade, L. (2006). A new initial rotor position detection technology based on HF injection and software PLL. School of Information Engineering. University of Science and Technology Beijing. DOI: 10.1109/ICICIC.2006.16. https://ieeexplore-ieee-org.ludwig.lub.lu.se/document/1691889?arnumber=1691889. Accessed on 2023-03-02.

Song, X., Han, B., Zheng, S., Chen, S. (2018). A Novel Sensorless Rotor Position Detection Method for High-Speed Surface PM Motors in a Wide Speed Range. DOI: 10.1109/TPEL.2017.2753289. https://ieeexplore-ieee-org.ludwig.lub.lu.se/document/8039267?arnumber=8039267. Accessed on 2023-06-14.

Surroop, D., Combes, P., Martin, P., and Rouchon, P., (2020). Sensorless rotor position estimation by PWM-induced signal injection. ISBN 978-1-7281-5414-5.

https://ieeexplore.ieee.org/document/9254909. Accessed on 2023-01-19.

Teske, N. (2001). Sensorless position control of induction machines using high frequency signal injection. Diss. University of Nottingham. ISNI: 0000 0001 3516 3625. https://ethos.bl.uk/OrderDetails.do?uin=uk.bl.ethos.367110. p107-110. Accessed on 2023-06-14.

Torrence, B.F., Torrence, E. (1999). The Student's Introduction to Mathematica. Cambridge University Press. ISBN 0-521-59461-8., p208

Rusek, F. (2021). Lecture 8: More about filters. EITF75 Systems and Signals 2020/2021. https://www.eit.lth.se/fileadmin/eit/courses/eitf75/2020/lecture8.pdf. Accessed on 2023-02-21.

Wenjun, X., Shaocheng, Q., Jinghong Z., Hongrui, Z., Xiaona, D. (2021). An Improved Full-Order Sliding-Mode Observer for Rotor Position and Speed Estimation of SPMSM. DOI: 10.1109/ACCESS.2021.3052085. https://ieeexplore.ieee.org/stamp/stamp.jsp?tp=&arnumber=9326370. Accessed on 2023-06-15.

Xiaocheng, W., Liang, Y., Zijian, J., Yuchen, Z., Pengjie, X. (2022). SPMSM Deadbeat Predictive Control with HF Injection Sensorless Rotor Position Estimate. 2022 IEEE 17th Conference on Industrial Electronics and Applications (ICIEA) Industrial Electronics and Applications (ICIEA), 2022 IEEE 17th Conference on. :920-925 Dec, 2022. DOI:10.1109/ICIEA54703.2022.10006068. https://ieeexplore-ieee-org.ludwig.lub.lu.se/stamp/stamp.jsp?tp=&arnumber=10006068. Accessed on 2023-06-16.

# 9 Appendix

## 9.1 Appendix A - Simulink implementation

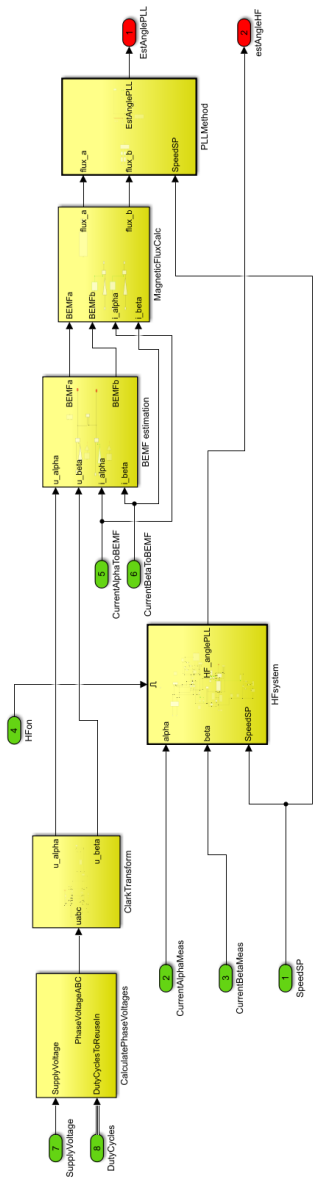


Figure 62: The overview of the implemented rotor position estimation algorithm.

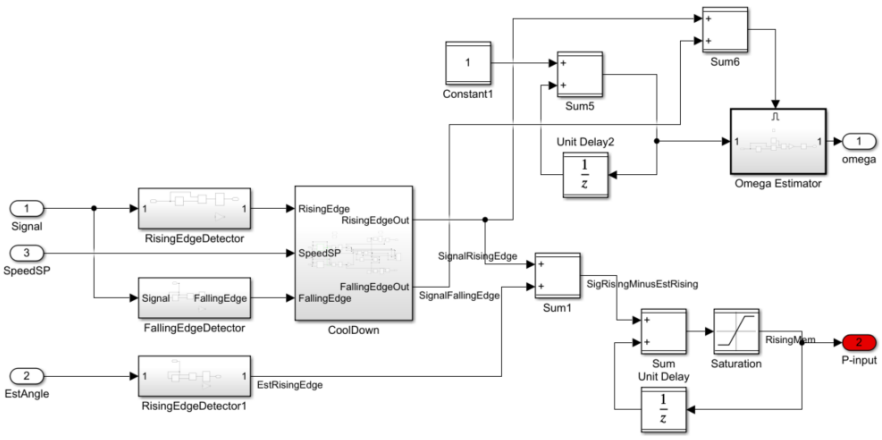


Figure 63: This figure shows the subsystem PFD that implements the phase frequency detection.

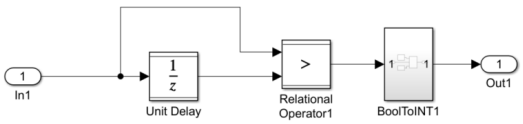


Figure 64: This figure shows the subsystem RisingEdgeDetector that detects if the square wave signal has a rising edge.

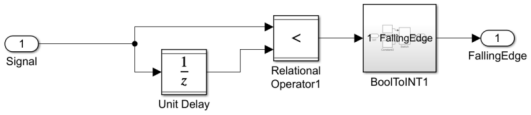


Figure 65: This figure shows the subsystem FallingEdgeDetector that detects if the square wave signal has a falling edge.

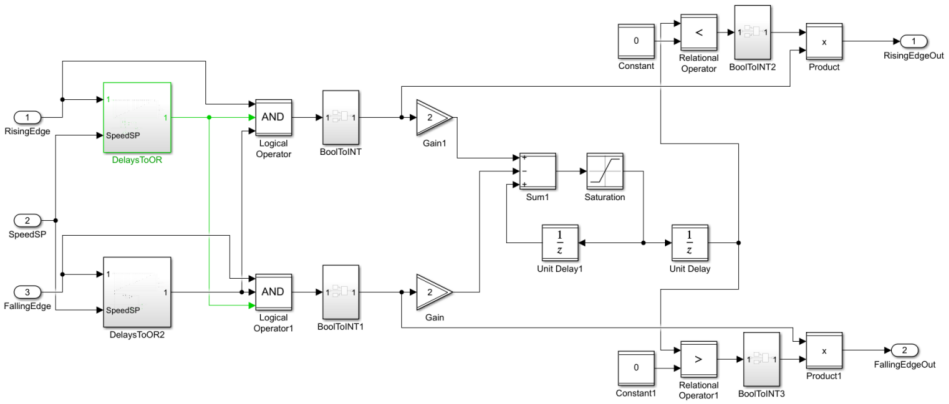


Figure 66: This figure shows the subsystem CoolDown that takes care of the noise in the input signal.

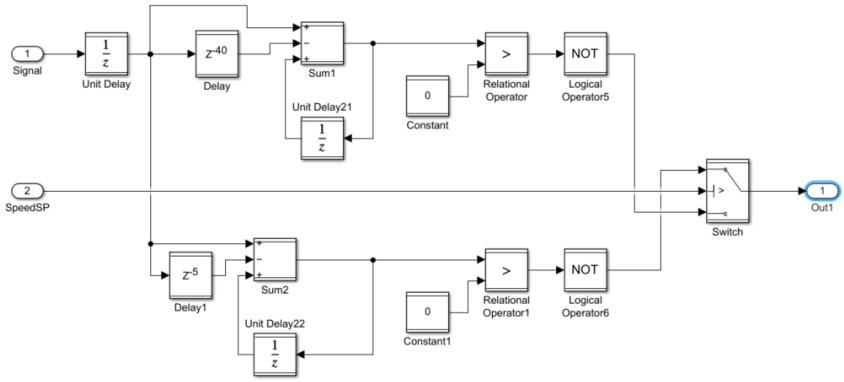


Figure 67: This figure shows the subsystem DelaysToOr that switches between using 5 or 40 latest samples of the signal depending on the speed reference.

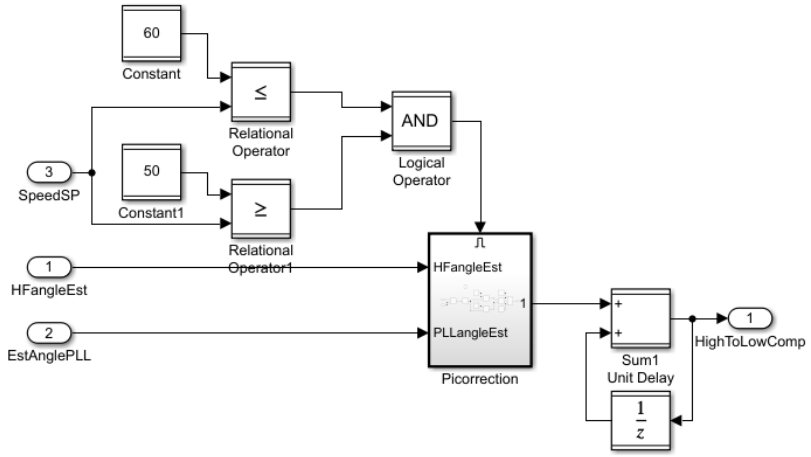


Figure 68: This figure shows the subsystem HighToLowSpeed that detects if the HF PLL have locked on the wrong phase when activating at 50 rad/s.

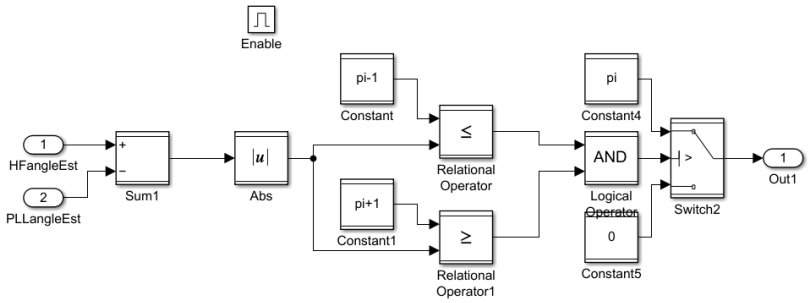


Figure 69: This figure shows the subsystem Pi-correction that is a part of the logic in figure 68, it detects if the HF PLL have locked on the wrong phase when activating at 50 rad/s.

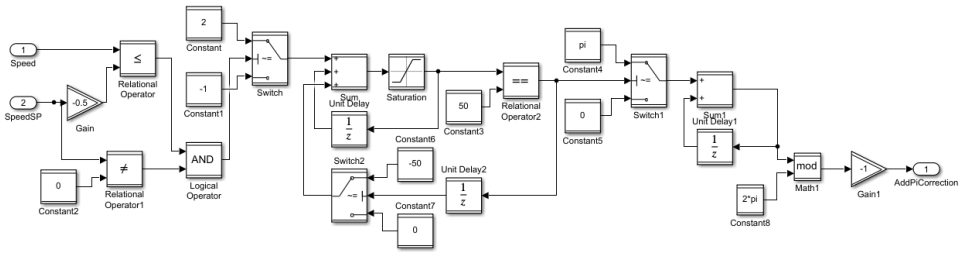


Figure 70: This figure shows the subsystem PolarityComp that will detect if the HF PLL have locked on the wrong phase primarily during the startup of the motor.